EUROPEAN LABORATORY FOR PARTICLE PHYSICS

CERN-PPE/97-083
14th June 1997

Search for Chargino and Neutralino Production at $\sqrt{s} = 170$ and 172 GeV at LEP

The OPAL Collaboration

Abstract

A search for charginos and neutralinos, predicted by supersymmetric theories, has been performed using a data sample of 10.3 pb^{-1} at centre-of-mass energies of $\sqrt{s}$ =170 and 172 GeV with the OPAL detector at LEP. No evidence for these particles has been found. The results are combined with those from previous OPAL chargino and neutralino searches at lower energies to obtain limits. Exclusion regions at 95% C.L. of parameters of the Minimal Supersymmetric Standard Model are determined. Within this framework, for $\tan\beta \geq 1.0$, lower mass limits are placed on the lightest chargino and the three lightest neutralinos. The 95% C.L. lower mass limit on the lightest chargino, assuming that it is heavier than the lightest neutralino by more than 10 GeV, is 84.5 GeV for the case of a large universal scalar mass ($m_0 > 1$ TeV) and 65.7 GeV for the smallest m_0 compatible with current limits on the sneutrino and slepton masses. The lower limit on the lightest neutralino mass at 95% C.L. for $\tan\beta \geq 1.0$ is 24.7 GeV for $m_0 = 1$ TeV and 13.3 GeV for the minimum m_0 scenario. These mass limits are higher for increasing values of $\tan\beta$. The interpretation of the limits in terms of gluino and scalar quark mass limits is also given.

Submitted to Zeit. Phys. C

The OPAL Collaboration

K. Ackerstaff[8], G. Alexander[23], J. Allison[16], N. Altekamp[5], K.J. Anderson[9], S. Anderson[12], S. Arcelli[2], S. Asai[24], D. Axen[29], G. Azuelos[18,a], A.H. Ball[17], E. Barberio[8], R.J. Barlow[16], R. Bartoldus[3], J.R. Batley[5], S. Baumann[3], J. Bechtluft[14], C. Beeston[16], T. Behnke[8], A.N. Bell[1], K.W. Bell[20], G. Bella[23], S. Bentvelsen[8], S. Bethke[14], O. Biebel[14], A. Biguzzi[5], S.D. Bird[16], V. Blobel[27], I.J. Bloodworth[1], J.E. Bloomer[1], M. Bobinski[10], P. Bock[11], D. Bonacorsi[2], M. Boutemeur[34], B.T. Bouwens[12], S. Braibant[12], L. Brigliadori[2], R.M. Brown[20], H.J. Burckhart[8], C. Burgard[8], R. Bürgin[10], P. Capiluppi[2], R.K. Carnegie[6], A.A. Carter[13], J.R. Carter[5], C.Y. Chang[17], D.G. Charlton[1,b], D. Chrisman[4], P.E.L. Clarke[15], I. Cohen[23], J.E. Conboy[15], O.C. Cooke[8], M. Cuffiani[2], S. Dado[22], C. Dallapiccola[17], G.M. Dallavalle[2], R. Davies[30], S. De Jong[12], L.A. del Pozo[4], K. Desch[3], B. Dienes[33,d], M.S. Dixit[7], E. do Couto e Silva[12], M. Doucet[18], E. Duchovni[26], G. Duckeck[34], I.P. Duerdoth[16], D. Eatough[16], J.E.G. Edwards[16], P.G. Estabrooks[6], H.G. Evans[9], M. Evans[13], F. Fabbri[2], M. Fanti[2], A.A. Faust[30], F. Fiedler[27], M. Fierro[2], H.M. Fischer[3], I. Fleck[8], R. Folman[26], D.G. Fong[17], M. Foucher[17], A. Fürtjes[8], D.I. Futyan[16], P. Gagnon[7], J.W. Gary[4], J. Gascon[18], S.M. Gascon-Shotkin[17], N.I. Geddes[20], C. Geich-Gimbel[3], T. Geralis[20], G. Giacomelli[2], P. Giacomelli[4], R. Giacomelli[2], V. Gibson[5], W.R. Gibson[13], D.M. Gingrich[30,a], D. Glenzinski[9], J. Goldberg[22], M.J. Goodrick[5], W. Gorn[4], C. Grandi[2], E. Gross[26], J. Grunhaus[23], M. Gruwé[8], C. Hajdu[32], G.G. Hanson[12], M. Hansroul[8], M. Hapke[13], C.K. Hargrove[7], P.A. Hart[9], C. Hartmann[3], M. Hauschild[8], C.M. Hawkes[5], R. Hawkings[27], R.J. Hemingway[6], M. Herndon[17], G. Herten[10], R.D. Heuer[8], M.D. Hildreth[8], J.C. Hill[5], S.J. Hillier[1], P.R. Hobson[25], R.J. Homer[1], A.K. Honma[28,a], D. Horváth[32,c], K.R. Hossain[30], R. Howard[29], P. Hüntemeyer[27], D.E. Hutchcroft[5], P. Igo-Kemenes[11], D.C. Imrie[25], M.R. Ingram[16], K. Ishii[24], A. Jawahery[17], P.W. Jeffreys[20], H. Jeremie[18], M. Jimack[1], A. Joly[18], C.R. Jones[5], G. Jones[16], M. Jones[6], U. Jost[11], P. Jovanovic[1], T.R. Junk[8], D. Karlen[6], V. Kartvelishvili[16], K. Kawagoe[24], T. Kawamoto[24], P.I. Kayal[30], R.K. Keeler[28], R.G. Kellogg[17], B.W. Kennedy[20], J. Kirk[29], A. Klier[26], S. Kluth[8], T. Kobayashi[24], M. Kobel[10], D.S. Koetke[6], T.P. Kokott[3], M. Kolrep[10], S. Komamiya[24], T. Kress[11], P. Krieger[6], J. von Krogh[11], P. Kyberd[13], G.D. Lafferty[16], R. Lahmann[17], W.P. Lai[19], D. Lanske[14], J. Lauber[15], S.R. Lautenschlager[31], J.G. Layter[4], D. Lazic[22], A.M. Lee[31], E. Lefebvre[18], D. Lellouch[26], J. Letts[12], L. Levinson[26], S.L. Lloyd[13], F.K. Loebinger[16], G.D. Long[28], M.J. Losty[7], J. Ludwig[10], A. Macchiolo[2], A. Macpherson[30], M. Mannelli[8], S. Marcellini[2], C. Markus[3], A.J. Martin[13], J.P. Martin[18], G. Martinez[17], T. Mashimo[24], P. Mättig[3], W.J. McDonald[30], J. McKenna[29], E.A. Mckigney[15], T.J. McMahon[1], R.A. McPherson[8], F. Meijers[8], S. Menke[3], F.S. Merritt[9], H. Mes[7], J. Meyer[27], A. Michelini[2], G. Mikenberg[26], D.J. Miller[15], A. Mincer[22,e], R. Mir[26], W. Mohr[10], A. Montanari[2], T. Mori[24], M. Morii[24], U. Müller[3], S. Mihara[24], K. Nagai[26], I. Nakamura[24], H.A. Neal[8], B. Nellen[3], R. Nisius[8], S.W. O'Neale[1], F.G. Oakham[7], F. Odorici[2], H.O. Ogren[12], A. Oh[27], N.J. Oldershaw[16], M.J. Oreglia[9], S. Orito[24], J. Pálinkás[33,d], G. Pásztor[32], J.R. Pater[16], G.N. Patrick[20], J. Patt[10], M.J. Pearce[1], R. Perez-Ochoa8, S. Petzold[27], P. Pfeifenschneider[14], J.E. Pilcher[9], J. Pinfold[30], D.E. Plane[8], P. Poffenberger[28], B. Poli[2], A. Posthaus[3], D.L. Rees[1], D. Rigby[1], S. Robertson[28], S.A. Robins[22], N. Rodning[30], J.M. Roney[28], A. Rooke[15], E. Ros[8], A.M. Rossi[2], P. Routenburg[30], Y. Rozen[22], K. Runge[10], O. Runolfsson[8], U. Ruppel[14], D.R. Rust[12], R. Rylko[25], K. Sachs[10], T. Saeki[24], E.K.G. Sarkisyan[23], C. Sbarra[29], A.D. Schaile[34], O. Schaile[34], F. Scharf[3], P. Scharff-Hansen[8], P. Schenk[34], J. Schieck[11], P. Schleper[11], B. Schmitt[8], S. Schmitt[11], A. Schöning[8], M. Schröder[8], H.C. Schultz-Coulon[10], M. Schumacher[3],

C. Schwick[8], W.G. Scott[20], T.G. Shears[16], B.C. Shen[4], C.H. Shepherd-Themistocleous[8], P. Sherwood[15], G.P. Siroli[2], A. Sittler[27], A. Skillman[15], A. Skuja[17], A.M. Smith[8], G.A. Snow[17], R. Sobie[28], S. Söldner-Rembold[10], R.W. Springer[30], M. Sproston[20], K. Stephens[16], J. Steuerer[27], B. Stockhausen[3], K. Stoll[10], D. Strom[19], P. Szymanski[20], R. Tafirout[18], S.D. Talbot[1], S. Tanaka[24], P. Taras[18], S. Tarem[22], R. Teuscher[8], M. Thiergen[10], M.A. Thomson[8], E. von Törne[3], S. Towers[6], I. Trigger[18], Z. Trócsányi[33], E. Tsur[23], A.S. Turcot[9], M.F. Turner-Watson[8], P. Utzat[11], R. Van Kooten[12], M. Verzocchi[10], P. Vikas[18], E.H. Vokurka[16], H. Voss[3], F. Wäckerle[10], A. Wagner[27], C.P. Ward[5], D.R. Ward[5], P.M. Watkins[1], A.T. Watson[1], N.K. Watson[1], P.S. Wells[8], N. Wermes[3], J.S. White[28], B. Wilkens[10], G.W. Wilson[27], J.A. Wilson[1], G. Wolf[26], T.R. Wyatt[16], S. Yamashita[24], G. Yekutieli[26], V. Zacek[18], D. Zer-Zion[8]

[1]School of Physics and Space Research, University of Birmingham, Birmingham B15 2TT, UK
[2]Dipartimento di Fisica dell' Università di Bologna and INFN, I-40126 Bologna, Italy
[3]Physikalisches Institut, Universität Bonn, D-53115 Bonn, Germany
[4]Department of Physics, University of California, Riverside CA 92521, USA
[5]Cavendish Laboratory, Cambridge CB3 0HE, UK
[6] Ottawa-Carleton Institute for Physics, Department of Physics, Carleton University, Ottawa, Ontario K1S 5B6, Canada
[7]Centre for Research in Particle Physics, Carleton University, Ottawa, Ontario K1S 5B6, Canada
[8]CERN, European Organisation for Particle Physics, CH-1211 Geneva 23, Switzerland
[9]Enrico Fermi Institute and Department of Physics, University of Chicago, Chicago IL 60637, USA
[10]Fakultät für Physik, Albert Ludwigs Universität, D-79104 Freiburg, Germany
[11]Physikalisches Institut, Universität Heidelberg, D-69120 Heidelberg, Germany
[12]Indiana University, Department of Physics, Swain Hall West 117, Bloomington IN 47405, USA
[13]Queen Mary and Westfield College, University of London, London E1 4NS, UK
[14]Technische Hochschule Aachen, III Physikalisches Institut, Sommerfeldstrasse 26-28, D-52056 Aachen, Germany
[15]University College London, London WC1E 6BT, UK
[16]Department of Physics, Schuster Laboratory, The University, Manchester M13 9PL, UK
[17]Department of Physics, University of Maryland, College Park, MD 20742, USA
[18]Laboratoire de Physique Nucléaire, Université de Montréal, Montréal, Quebec H3C 3J7, Canada
[19]University of Oregon, Department of Physics, Eugene OR 97403, USA
[20]Rutherford Appleton Laboratory, Chilton, Didcot, Oxfordshire OX11 0QX, UK
[22]Department of Physics, Technion-Israel Institute of Technology, Haifa 32000, Israel
[23]Department of Physics and Astronomy, Tel Aviv University, Tel Aviv 69978, Israel
[24]International Centre for Elementary Particle Physics and Department of Physics, University of Tokyo, Tokyo 113, and Kobe University, Kobe 657, Japan
[25]Brunel University, Uxbridge, Middlesex UB8 3PH, UK
[26]Particle Physics Department, Weizmann Institute of Science, Rehovot 76100, Israel
[27]Universität Hamburg/DESY, II Institut für Experimental Physik, Notkestrasse 85, D-22607 Hamburg, Germany
[28]University of Victoria, Department of Physics, P O Box 3055, Victoria BC V8W 3P6, Canada

[29]University of British Columbia, Department of Physics, Vancouver BC V6T 1Z1, Canada
[30]University of Alberta, Department of Physics, Edmonton AB T6G 2J1, Canada
[31]Duke University, Dept of Physics, Durham, NC 27708-0305, USA
[32]Research Institute for Particle and Nuclear Physics, H-1525 Budapest, P O Box 49, Hungary
[33]Institute of Nuclear Research, H-4001 Debrecen, P O Box 51, Hungary
[34]Ludwigs-Maximilians-Universität München, Sektion Physik, Am Coulombwall 1, D-85748 Garching, Germany

[a] and at TRIUMF, Vancouver, Canada V6T 2A3
[b] and Royal Society University Research Fellow
[c] and Institute of Nuclear Research, Debrecen, Hungary
[d] and Department of Experimental Physics, Lajos Kossuth University, Debrecen, Hungary
[e] and Department of Physics, New York University, NY 1003, USA

1 Introduction

When unification of the electromagnetic, weak, and strong forces in the Standard Model is considered, a severe problem exists in the understanding of the enormous ratio between the energy scales of full unification of the three forces and the scale of unification of the electromagnetic and weak forces. This "naturalness" or "gauge hierarchy" problem must be addressed by any new theory that attempts to unify the fundamental forces. One of the most promising candidates for this new physics is the theory of supersymmetry (SUSY) [1] that extends the Standard Model with a new type of symmetry between fermions and bosons that also allows for the incorporation of the gravitational force.

In October and November 1996 the LEP e^+e^- collider at CERN was run at the new centre-of-mass energies ($\sqrt{s}$) of 170 and 172 GeV, thus expanding the kinematically accessible region for new particle searches. A direct search for charginos and neutralinos predicted in SUSY theories [1] is described using the data collected with the OPAL detector. The large predicted cross section for chargino production leads to excellent discovery potential for this SUSY particle with the present integrated luminosity collected at LEP2. More stringent exclusion mass and cross-section limits are obtained compared to the previous results from the analysis of data near the Z peak (LEP1), at $\sqrt{s} = 130$ GeV and 136 GeV (LEP1.5) and at $\sqrt{s} = 161$ GeV by the OPAL [2, 3] and the other LEP collaborations [4]. The search for charginos is similar to that described in [3] while a new and more efficient method has been incorporated for the neutralino search. Similar, but more model-dependent, limits have been obtained by the CDF and D0 collaborations at the Tevatron $p\bar{p}$ collider [5].

Charginos, $\tilde{\chi}_j^{\pm}$, are the mass eigenstates formed by the mixing of the fields of the fermionic partners of the W boson (winos) and those of the charged Higgs bosons (charged higgsinos). Fermionic partners of the γ, the Z boson, and the neutral Higgs bosons mix to form mass eigenstates called neutralinos, $\tilde{\chi}_i^0$. In each case, the index j or i is ordered by increasing mass. R-parity [6] conservation is assumed; therefore, the lightest supersymmetric particle (LSP) is stable. The LSP is usually considered to be the lightest neutralino, $\tilde{\chi}_1^0$, although it could be the scalar neutrino, $\tilde{\nu}$, if it is sufficiently light. It escapes detection due to its weakly interacting nature. The present analysis is valid in either case.

The Minimal Supersymmetric Standard Model (MSSM) [7] is used to guide the analysis but more general cases are also studied. In the MSSM two chargino mass eigenstates ($\tilde{\chi}_1^{\pm}$ and $\tilde{\chi}_2^{\pm}$) and four neutralino mass eigenstates ($\tilde{\chi}_1^0$, $\tilde{\chi}_2^0$, $\tilde{\chi}_3^0$ and $\tilde{\chi}_4^0$) are expected to exist.

If charginos exist and are sufficiently light, they will be pair-produced in e^+e^- collisions through a γ or Z in the s-channel. For the wino component there is an additional production process through scalar electron neutrino (electron sneutrino, $\tilde{\nu}_e$) exchange in the t-channel. The production cross-section is large unless the sneutrino is light, in which case the cross-section is reduced by destructive interference between the s-channel e^+e^- annihilation to Z or γ and t-channel $\tilde{\nu}_e$ exchange diagrams [8, 9]. The details of chargino decay depend on the parameters of the mixing and the masses of the scalar partners of the ordinary fermions. The lightest chargino $\tilde{\chi}_1^+$ can decay into $\tilde{\chi}_1^0 \ell^+ \nu$, or $\tilde{\chi}_1^0 q\overline{q}'$, via a virtual W, scalar lepton (slepton, $\tilde{\ell}$), sneutrino ($\tilde{\nu}$) or scalar quark (squark, $\tilde{q}$). In much of the MSSM parameter space $\tilde{\chi}_1^+$ decays via a virtual W are dominant. In the MSSM, the predicted cross-section for $\tilde{\chi}_1^+\tilde{\chi}_1^-$ pair production is typically several pb. Due to the energy and momentum carried away by the invisible $\tilde{\chi}_1^0$ and/or neutrinos, the experimental signature for $\tilde{\chi}_1^+\tilde{\chi}_1^-$ events is large missing energy and large missing momentum transverse to the beam axis.

Neutralino pairs ($\tilde{\chi}_1^0\tilde{\chi}_2^0$) can be produced through an s-channel virtual Z or γ, or by t-channel scalar electron (selectron, $\tilde{\mathrm{e}}$) exchange [11]. The $\tilde{\chi}_2^0$ will decay into the final states[1] $\tilde{\chi}_1^0\nu\bar{\nu}$, $\tilde{\chi}_1^0\ell^+\ell^-$ or $\tilde{\chi}_1^0\mathrm{q}\bar{\mathrm{q}}$. For the latter two cases this leads to an experimental signature consisting either of an acoplanar pair of particles or jets, or a monojet in which the two jets in the final state have merged. In some regions of SUSY parameter space the radiative decay process $\tilde{\chi}_2^0 \to \tilde{\chi}_1^0\gamma$ is also possible [10]. The MSSM predicted cross-sections for $\tilde{\chi}_2^0\tilde{\chi}_1^0$ events can vary significantly depending on the choice of MSSM parameters. They are typically a fraction of a pb and generally much less than the cross-section for $\tilde{\chi}_1^-\tilde{\chi}_1^+$ production. In the MSSM analyses reported here all possible cascade decay processes [11, 12] are taken into account. For example, $\tilde{\chi}_3^0$ decays into $\tilde{\chi}_{1,2}^0\mathrm{Z}^*$ are considered as well as $\tilde{\chi}_3^0$ decays into $\tilde{\chi}_{1,2}^0\mathrm{h}^0$ and $\tilde{\chi}_{1,2}^0\mathrm{A}^0$ and decays where $\tilde{\chi}_3^0 \to \tilde{\chi}_2^0\gamma$ with $\tilde{\chi}_2^0 \to \tilde{\chi}_1^0\mathrm{Z}^*$. Therefore, the experimental signatures for $\tilde{\chi}_1^0\tilde{\chi}_3^0$ events are somewhat similar to those for $\tilde{\chi}_1^0\tilde{\chi}_2^0$. $\tilde{\chi}_2^0\tilde{\chi}_2^0$ pairs can also be produced, but as limits on their production do not affect the limits placed on the MSSM parameter space (CMSSM, see below) they are not considered in this analysis.

Within the framework of the MSSM the mass spectra and couplings of charginos and neutralinos are mainly determined by the following four parameters: the ratio of the vacuum expectation values of the two Higgs doublets ($\tan\beta$), the U(1) and SU(2) gaugino mass parameters at the weak scale (M_1 and M_2), and the mixing parameter of the two Higgs doublet fields (μ). Assuming Grand Unification (GUT), all gauginos (supersymmetric partners of the gauge bosons) have a common mass $m_{1/2}$ at the GUT mass scale. The gaugino masses at the weak scale are determined by the renormalization group equations. As a result, the ratios of the U(1), SU(2) and SU(3) gaugino masses (M_1:M_2:M_3) are equal to α_1:α_2:α_3, where α_i ($i = 1, 2, 3$) are the strengths of the gauge couplings at the weak scale. If Grand Unification is assumed then $M_2 = 0.82\ m_{1/2}$. M_2 is conventionally chosen as an independent parameter.

Each sfermion mass at the GUT scale would be an additional parameter independent of $\tan\beta$, M_2 and μ. However, assuming a common sfermion mass, m_0, at the GUT scale, the sfermion masses run with a mass scale according to the renormalization group equations. Assuming a common gaugino mass and a common sfermion mass at the GUT scale within the framework of the MSSM leads to a model called constrained MSSM (CMSSM). The interpretation of the results in this publication is based on the CMSSM, although some results are valid in a larger framework. In this model the squark, slepton and sneutrino masses at the weak scale are approximately given by the following formulae[2] [13]:

$$m^2_{\tilde{\mathrm{u}}_R} = m_0^2 + 5.87\ m_{1/2}^2 - 0.16\ m_{\mathrm{Z}}^2|\cos 2\beta| \quad (1)$$

$$m^2_{\tilde{\mathrm{u}}_L} = m_0^2 + 6.28\ m_{1/2}^2 - 0.35\ m_{\mathrm{Z}}^2|\cos 2\beta| \quad (2)$$

$$m^2_{\tilde{\mathrm{d}}_R} = m_0^2 + 5.82\ m_{1/2}^2 + 0.08\ m_{\mathrm{Z}}^2|\cos 2\beta| \quad (3)$$

$$m^2_{\tilde{\mathrm{d}}_L} = m_0^2 + 6.28\ m_{1/2}^2 + 0.42\ m_{\mathrm{Z}}^2|\cos 2\beta| \quad (4)$$

$$m^2_{\tilde{\ell}_R} = m_0^2 + 0.15\ m_{1/2}^2 + 0.23\ m_{\mathrm{Z}}^2|\cos 2\beta| \quad (5)$$

$$m^2_{\tilde{\ell}_L} = m_0^2 + 0.52\ m_{1/2}^2 + 0.27\ m_{\mathrm{Z}}^2|\cos 2\beta| \quad (6)$$

$$m^2_{\tilde{\nu}_L} = m_0^2 + 0.52\ m_{1/2}^2 - 0.50\ m_{\mathrm{Z}}^2|\cos 2\beta|, \quad (7)$$

[1] The decay would be via a Z^*, a neutral SUSY Higgs boson (h^0 or A^0), sneutrino, slepton, or squark. The decay via Z^* is the dominant mode in most of the parameter space.

[2] These formulae cannot be directly applied for the masses of the stop, sbottom and stau, since these are affected by the large corrections due to $\tilde{\mathrm{f}}_\mathrm{L}$-$\tilde{\mathrm{f}}_\mathrm{R}$ mixing. More accurate formulae for the sfermion masses are provided in [14].

where the last term in each expression is zero for $\tan\beta = 1$. Limits in the (M_2,μ) parameter space, obtained from the chargino and neutralino searches, are presented for $\tan\beta = 1.5$ and 35. These two values of $\tan\beta$ are theoretically interesting since at these values the model is consistent with both the measured value of the top mass and the mass ratio of the τ and the bottom quark. However, $\tan\beta$ could be as small as 1.0 [15]. The phenomenology of chargino and neutralino production and decay changes drastically when $\tan\beta$ approaches 1.0. Therefore the case of $\tan\beta = 1.0$ is also studied.

For $\tan\beta$ close to 1.0, the ordinary analysis based on large missing momentum is insensitive in the region $M_2 \approx \mu \approx 0$ of the (M_2,μ) plane. In this region the two chargino masses are close to the mass of the W boson ($m_{\tilde{\chi}_1^\pm} \approx m_{\tilde{\chi}_2^\pm} \approx m_{\mathrm{W}}$), the two lightest neutralinos are almost massless[3] ($m_{\tilde{\chi}_1^0} \approx m_{\tilde{\chi}_2^0} \approx 0$), and the other two neutralino masses are close to the mass of the Z boson ($m_{\tilde{\chi}_3^0} \approx m_{\tilde{\chi}_4^0} \approx m_{\mathrm{Z}}$). In this region one of the two lightest neutralinos is an almost pure photino and the other one is an almost pure higgsino, hence $\tilde{\chi}_1^0\tilde{\chi}_2^0$ production in $\mathrm{e^+e^-}$ collisions is heavily suppressed. The heavy neutralinos $\tilde{\chi}_3^0$ and $\tilde{\chi}_4^0$ are mixtures of the zino and the other higgsino. To be sensitive to the region near $M_2 = \mu = 0$, the ALEPH collaboration has studied $\tilde{\chi}_2^0\tilde{\chi}_3^0$ or $\tilde{\chi}_2^0\tilde{\chi}_4^0$ production with the subsequent decays $\tilde{\chi}_{3,4}^0 \to \mathrm{Z}^{(*)}\tilde{\chi}_2^0$ and $\tilde{\chi}_2^0 \to \tilde{\chi}_1^0\gamma$ at centre-of-mass energies $\sqrt{s} = 130$ and 136 GeV [16]. At these energies charginos are too heavy to be produced in the considered parameter region. At $\sqrt{s}$ well above the W-pair threshold, the chargino pair production cross-section is typically much larger than the neutralino pair ($\tilde{\chi}_2^0\tilde{\chi}_3^0$ or $\tilde{\chi}_2^0\tilde{\chi}_4^0$) production cross-sections near $M_2 = \mu = 0$. At $\sqrt{s} = 172$ GeV, the sum of the cross-sections for the four chargino pair production processes ($\mathrm{e^+e^-} \to \tilde{\chi}_1^+\tilde{\chi}_1^-$, $\tilde{\chi}_2^+\tilde{\chi}_2^-$ and $\tilde{\chi}_1^\pm\tilde{\chi}_2^\mp$) near $M_2 = \mu = 0$ is as large as 6 pb, whereas the $\mathrm{W^+W^-}$ production cross-section is about 13 pb.

In the (M_2,μ) region considered here, the event shapes of the chargino pair events ($\tilde{\chi}_1^+\tilde{\chi}_1^-$, $\tilde{\chi}_2^+\tilde{\chi}_2^-$ or $\tilde{\chi}_1^\pm\tilde{\chi}_2^\mp$) are similar to those of ordinary $\mathrm{W^+W^-}$ events, since each chargino decays into an on-mass-shell or almost on-mass-shell W with an almost massless neutralino having low momentum. These events tend to have somewhat larger missing energy than the ordinary W pair events, since the neutralinos tend to have small, but significant, momentum. A large neutralino momentum in the rest frame of the chargino is favoured due to the larger phase space available in the two-body decay $\tilde{\chi}_i^\pm \to \mathrm{W}^{(*)^+}\tilde{\chi}_j^0$. On the other hand, the W boson tends to stay near its mass-shell. These two effects determine the momentum spectrum of the neutralinos. A search for an excess of $\mathrm{W^+W^-}$-like events with respect to the Standard Model expectation (mainly pairs of W bosons) is performed. For a sneutrino mass smaller than about 100 GeV the chargino pair production cross-section is reduced due to the negative interference between s-channel annihilation into γ or Z and t-channel $\tilde{\nu}_\mathrm{e}$ exchange diagrams. Hence for a small sneutrino mass the region of low sensitivity in the (M_2,μ) plane becomes significantly large. The present analysis has therefore been designed in such a way that a relatively large region around $M_2 = \mu = 0$ is covered. The charginos ($\tilde{\chi}_1^\pm$ and $\tilde{\chi}_2^\pm$) decay either into $\tilde{\chi}_1^0\mathrm{W}^{(*)^\pm}$ or $\tilde{\chi}_2^0\mathrm{W}^{(*)^\pm}$. The light $\tilde{\chi}_2^0$ decays subsequently into $\tilde{\chi}_1^0\gamma$ through loop diagrams. If the sneutrino is lighter than the chargino, the two-body decay $\tilde{\chi}^\pm \to \tilde{\nu}_\ell\ell^\pm$ would dominate, but the subsequent decay of $\tilde{\nu}_\ell \to \nu_\ell\tilde{\chi}_j^0$ leads to the same final state topology as the leptonic decay via $\tilde{\chi}_j^0\mathrm{W}^{(*)^\pm}$. The SUSYGEN Monte Carlo generator [17] is used to calculate these branching fractions.

In this publication, the OPAL detector is described in Section 2. The various event simulations which have been used are described in Section 3. Analyses of the various possible

[3]Small gluino masses have not been considered here.

signal topologies are discussed in Section 4 and results and physics interpretations, both model independent and based on the CMSSM, are given in Section 5.

2 The OPAL Detector

The OPAL detector is described in detail in [18]; it is a multipurpose apparatus having nearly complete solid angle coverage[4]. The central tracking system consists of a silicon microvertex detector, a vertex drift chamber, a jet chamber and z-chambers. In the range $|\cos\theta| < 0.73$, 159 points can be measured in the jet chamber along each track. At least 20 points on a track can be obtained over 96% of the full solid angle. The whole tracking system is located inside a 0.435 T axial magnetic field. A lead-glass electromagnetic (EM) calorimeter providing acceptance within $|\cos\theta| < 0.984$ together with presamplers and time-of-flight scintillators is located outside the magnet coil and at the front of both endcaps. The magnet return yoke is instrumented for hadron calorimetry (HCAL) giving a polar angle coverage of $|\cos\theta| < 0.99$ and is surrounded by external muon chambers. The forward detectors (FD) and silicon tungsten calorimeters[5] (SW) located on both sides of the interaction point measure the luminosity and complete the geometrical acceptance down to 24 mrad in polar angle. The gap between the endcap EM calorimeter and FD is filled by an additional electromagnetic calorimeter, called the gamma-catcher (GC).

3 Event Simulation

The DFGT generator [19] was used to simulate signal events. It includes spin correlations and allows a proper treatment of the W boson width effect in the chargino decay, in particular when the chargino decays into quasi-on-mass-shell W bosons as in the case of $\tan\beta = 1.0$ with $M_2 \approx \mu \approx 0$.

The results obtained using the DFGT generator were cross-checked using the SUSYGEN generator [17]. Both generators include initial state radiation. The JETSET 7.4 package [20] is used for the hadronisation of the quark-antiquark system in the chargino or neutralino hadronic decays. It is important to incorporate correctly all the possible branching fractions of charginos and neutralinos. SUSYGEN is used to calculate these branching fractions.

The most important parameters influencing the chargino detection efficiency are the mass of the lightest chargino, $m_{\tilde{\chi}_1^+}$, and the mass difference between the lightest chargino and the lightest neutralino, $\Delta M_+ \equiv m_{\tilde{\chi}_1^+} - m_{\tilde{\chi}_1^0}$. For the neutralino detection efficiency, $m_{\tilde{\chi}_2^0}$ and $\Delta M_0 \equiv m_{\tilde{\chi}_2^0} - m_{\tilde{\chi}_1^0}$ are the main parameters that affect the efficiency. For $\tilde{\chi}_1^+\tilde{\chi}_1^-$ events, 64 points were generated in the ($m_{\tilde{\chi}_1^+}$,ΔM_+) plane, for $m_{\tilde{\chi}_1^+}$ between 50 GeV and 85 GeV and ΔM_+ between 3 GeV and $m_{\tilde{\chi}_1^+}$, in the wino-higgsino mixed case and in the pure higgsino case. The correspondence of these cases to the MSSM parameters is explained in Section 5.2.

[4] A right-handed coordinate system is adopted, where the x-axis points to the centre of the LEP ring, and positive z is along the electron beam direction. The angles θ and ϕ are the polar and azimuthal angles, respectively.

[5] In 1996, tungsten shields were installed around the beam pipe in front of the SW detectors to reduce the amount of synchrotron radiation seen by the detector. The presence of the shield results in a hole in the SW acceptance between the polar angles of 28 and 31 mrads.

To study systematic effects due to variations in the matrix element which lead to different production and decay angular distributions, events were generated at 32 additional points in the pure wino case. At each point 1000 events for the decay $\tilde{\chi}_1^+ \to \tilde{\chi}_1^0 \mathrm{W}^{*+}$ were generated. For $\tilde{\chi}_1^0\tilde{\chi}_2^0$ events, 62 points were generated in the ($m_{\tilde{\chi}_1^0}$,$m_{\tilde{\chi}_2^0}$) plane, for ($m_{\tilde{\chi}_1^0} + m_{\tilde{\chi}_2^0}$) between 100 GeV and 170 GeV and $m_{\tilde{\chi}_1^0}$ between 10 GeV and ($m_{\tilde{\chi}_2^0} - 3.0$ GeV). At each point, 1000 events for the decay $\tilde{\chi}_2^0 \to \tilde{\chi}_1^0 \mathrm{Z}^*$ with $\mathrm{Z}^* \to \ell^+\ell^-$ or $\mathrm{q\bar{q}}$ were generated.

The sources of background to the chargino and neutralino signals include two-photon, lepton-pair, multihadronic and four-fermion processes. Two-photon processes are the most important background for the case of small ΔM_+ where the visible energy and momentum transverse to the beam direction for the signal and the two-photon events are comparable. The Monte Carlo generators PYTHIA [20], PHOJET [21] and HERWIG [22] were used for simulating hadronic events from two-photon processes. Other four-fermion processes, excluding $\mathrm{e^+e^-e^+e^-}$, were simulated using the grc4f [23] generator, which takes into account all interfering four-fermion diagrams. The dominant contributions are $\mathrm{W^+W^-}$, $\mathrm{Z}\gamma^*$ or $\mathrm{Z^*Z}$ events that have topologies very similar to that of the signal. The Vermaseren [24] program was used to simulate $\mathrm{e^+e^-e^+e^-}$, as well as additional samples of $\mathrm{e^+e^-}\mu^+\mu^-$ and $\mathrm{e^+e^-}\tau^+\tau^-$ processes. The EXCALIBUR [25] program was used as a cross-check. Lepton pairs were generated using the KORALZ [26] generator for $\tau^+\tau^-(\gamma)$ and $\mu^+\mu^-(\gamma)$ events and the BHWIDE [27] program for $\mathrm{e^+e^-} \to \mathrm{e^+e^-}(\gamma)$ events. Multihadronic, $\mathrm{q\bar{q}}(\gamma)$, events were simulated using PYTHIA.

The simulated background events were all generated at $\sqrt{s} = 171.0$ GeV. In evaluating the number of background events, the cross-sections were calculated at the actual centre-of-mass energies (170.3 GeV and 172.3 GeV) and were weighted by the corresponding collected luminosities.

Generated signal and background events were processed through the full simulation of the OPAL detector [28] and the same event analysis chain was applied to the simulated events as to the data.

4 Analysis

The analysis is performed on data collected during the 1996 autumn run of LEP at centre-of-mass energies of $\sqrt{s}$ =170.3 and 172.3 GeV. Data are used from runs in which all the subdetectors relevant to this analysis were fully operational, corresponding to an integrated luminosity of 10.3 pb^{-1} (1.0 pb^{-1} at 170.3 GeV and 9.3 pb^{-1} at 172.3 GeV). The luminosity is measured using small angle Bhabha scattering events detected in the silicon tungsten calorimeter.

To select good charged tracks and clusters in the calorimeters, quality requirements identical to those in Ref. [2] are applied.

Calculations of experimental variables are performed using the four-momenta of tracks and of EM or HCAL clusters not associated with charged tracks[6]. Calorimeter clusters associated with charged tracks are also included after the expected calorimeter energy for the associated charged track momenta is subtracted from the cluster energy to reduce double counting. If the energy of a cluster is smaller than the expected energy for the associated tracks, the cluster energy is not used.

[6]The masses of all charged particles are set to the charged pion mass, and the invariant masses of the calorimeter energy clusters are assumed to be zero.

Jets are formed from charged tracks and calorimeter clusters using the Durham algorithm [29] with a jet resolution parameter of $y_{\rm cut} = 0.005$, unless otherwise specified.

To select well measured events the following preselection criteria are applied:

(P1) The number of charged tracks satisfying the quality criteria is required to be at least two. Furthermore, the ratio of the number of tracks satisfying the quality criteria to the total number of reconstructed tracks is required to be larger than 0.2.

(P2) The event transverse momentum relative to the beam direction is required to be larger than 1.8 GeV.

(P3) The total energy deposited in each side of the silicon tungsten calorimeter, forward calorimeter and the gamma-catcher has to be smaller than 2 GeV, 2 GeV and 5 GeV, respectively.

(P4) The visible invariant mass of the event has to exceed 3 GeV.

(P5) The maximum EM cluster energy and the maximum charged track momentum both have to be smaller than 130% of the beam energy.

After these preselection cuts 6310 data events are selected for further analysis compared with an expectation from the simulation of the relevant backgrounds of 5535 events. The difference between observed and expected events is attributed to the incomplete modelling of low mass two-photon processes by the available generators. As described later, reducing the two-photon contribution in the course of the analysis yields satisfactory agreement between data and background simulation.

4.1 Detection of charginos

For the chargino search, the event sample is divided into three categories, motivated by the topologies expected to result from chargino events. Separate analyses are applied to the preselected events in each category to obtain optimal performance:

(A) $N_{\rm ch} > 4$ and no isolated lepton observed, where $N_{\rm ch}$ is the number of reconstructed charged tracks,

(B) $N_{\rm ch} > 4$ and at least one isolated lepton observed, and

(C) $N_{\rm ch} \leq 4$.

For the preselected events 1448 are classified as (A), 1296 as (B) and 3566 as (C).

These analyses are similar to those used for the analysis of 161 GeV data [3] but their robustness to the larger $\rm W^+W^-$ background has been significantly improved.

Isolated leptons are identified in the following way. Electrons are selected if they satisfied either the artificial neural network electron identification described in [30] or the one used for the OPAL $R_{\rm b}$ analysis [31]. Muons are selected if they satisfied one of three muon identification methods: the first method is based on the best matching track to the muon chamber track

segment [32], the second on the use of the hadron calorimeter as described in [33] and the third one is applying the cuts used in the OPAL Z line shape analysis [34]. The momentum of the electron or muon candidate is required to be larger than 2 GeV. A reconstructed jet is identified as a tau decay if there are only one or three charged tracks in the jet, the momentum sum of the charged tracks is larger than 2 GeV, the invariant mass of the charged particles in the jet is smaller than 1.5 GeV and the invariant mass of the jet is smaller than the mass of the tau [36]. The lepton is defined to be isolated if the energy within a cone of half angle 20° around the electron, muon or tau candidate is less than 2 GeV.

The fractions of $\tilde{\chi}_1^+\tilde{\chi}_1^-$ events falling into categories (A), (B) and (C) for various mass combinations of ($m_{\tilde{\chi}_1^0}$, $m_{\tilde{\chi}_1^\pm}$) are given in Table 1.

To complete the chargino search in a particular region of SUSY parameter space ($M_2 \approx \mu \approx 0$ for $\tan\beta = 1$) which is not accessible by analyses (A), (B) and (C), two additional analyses described in Section 4.3 are performed.

$\tilde{\chi}_1^+\tilde{\chi}_1^-$	$m_{\tilde{\chi}_1^+}$	50 GeV	60 GeV	65 GeV	70 GeV	75 GeV	80 GeV	85 GeV
ΔM_+	Category							
3.0 GeV	(A)	3	3	3	3	5	5	7
	(B)	10	11	10	10	9	8	7
	(C)	87	86	88	87	87	87	86
5.0 GeV	(A)	12	9	8	7	7	8	7
	(B)	32	32	35	37	37	34	38
	(C)	56	59	57	56	56	58	55
10.0 GeV	(A)	28	20	20	17	15	13	12
	(B)	45	50	55	53	55	55	61
	(C)	27	30	25	30	30	32	27
20.0 GeV	(A)	38	36	36	34	33	30	32
	(B)	46	47	50	49	50	53	50
	(C)	16	17	14	17	17	17	18
$m_{\tilde{\chi}_1^+}/2$	(A)	42	45	44	45	48	50	49
	(B)	44	43	41	43	39	39	40
	(C)	15	12	16	13	13	10	11
$m_{\tilde{\chi}_1^+}$	(A)	45	44	50	51	50	53	54
-20 GeV	(B)	40	43	40	36	38	35	35
	(C)	15	13	10	13	12	12	11
$m_{\tilde{\chi}_1^+}$	(A)	48	51	50	49	54	54	59
-10 GeV	(B)	39	37	36	38	36	34	32
	(C)	13	11	13	13	11	11	9
$m_{\tilde{\chi}_1^+}$	(A)	53	51	54	53	53	56	57
	(B)	36	38	34	36	37	34	33
	(C)	11	11	11	11	10	10	10

Table 1: The percentages of the simulated $\tilde{\chi}_1^+\tilde{\chi}_1^-$ event samples falling into each of the three categories for $\tilde{\chi}_1^\pm \to \tilde{\chi}_1^0 \mathrm{W}^{*\pm}$ decay, where $\Delta M_+ = m_{\tilde{\chi}_1^+} - m_{\tilde{\chi}_1^0}$. These percentages have been evaluated using 1000 events for each mass combination.

4.1.1 Analysis A ($N_{\rm ch} > 4$ without isolated leptons)

For reasonably large values of ΔM_+, if both $\tilde{\chi}_1^+$ and $\tilde{\chi}_1^-$ decay hadronically, signal events tend to fall into category (A). As listed in Table 1, the fraction of $\tilde{\chi}_1^+\tilde{\chi}_1^-$ events falling into category (A) is 30–59% if ΔM_+ is 20 GeV or greater. The fraction drops to less than or equal to 12% for $\Delta M_+ \leq 5$ GeV since the average charged track multiplicity of these events is small.

For an event to be considered as a candidate it has to satisfy the following criteria:

(A1) To ensure that the events are well contained, a requirement is imposed on the direction of the missing momentum ($|\cos\theta_{\rm miss}| < 0.9$). Furthermore, the ratio of the measured energy in the forward cones (defined by $|\cos\theta| > 0.9$) to the total measured energy should be smaller than 15%.

(A2) The background from multihadronic two-photon processes is strongly reduced by imposing a cut on the total transverse momentum of the event including ($P_t^{\rm HCAL} > 6$ GeV) and not including ($P_t > 5$ GeV) the information from the hadron calorimeter. Although most of the events from two-photon processes are rejected by the P_t cut, the $P_t^{\rm HCAL}$ cut is applied to reject two-photon events with an occasional high transverse momentum neutral hadron. In addition, the longitudinal component of the missing momentum is required to be smaller than 35 GeV, which reduces the contribution from radiative Z events.

(A3) To reject multihadronic annihilation and $\rm W^+W^-$ final states, further requirements are imposed on the acoplanarity and measured mass of the event. The event is divided into two jets using the Durham jet algorithm. The acoplanarity angle, $\phi_{\rm acop}$, is defined as the complement of the azimuthal opening angle of the two jets, each of which should be well contained ($|\cos\theta| < 0.95$). Figure 1 shows the acoplanarity angle distribution for the data and the various background components, and for various signals. The acoplanarity angle should exceed 15°. Furthermore, the total observed mass of the event should be smaller than 100 GeV.

(A4) Remaining $\rm W^+W^-$ events where one W decays semileptonically are rejected by using a different lepton algorithm which has less stringent isolation criteria [3]. Events containing a lepton of this type, with a hadronic system recoiling against it with a reconstructed mass between 55 to 85 GeV are rejected.

Events are then classified according to the number of hadronic jets. Figure 2(a) shows the number of hadronic jets versus reconstructed invariant mass for $\ell^+\ell^-\rm q\bar{q}$, $\nu\ell\rm q\bar{q}'$ and $\nu\bar{\nu}\rm q\bar{q}$ final state background events that are the dominant background processes at this stage. Most of the events fall into the two- and three-jet topologies. Figures 2(b) and (c) show the same distributions for the expected signal events in the case of small ΔM_+ and large ΔM_+, respectively. It can be seen that while the low ΔM_+ case is dominated by low masses and two or three jets, the large ΔM_+ case is dominated by four-jet events with large invariant mass. To preserve high detection efficiency for both large and small ΔM_+, the analysis is divided into two parts.

In the first part, two- and three-jet events are selected, and the following requirements are imposed:

(A5a) Highly boosted events satisfying $M_{\rm vis}/E_{\rm vis} < 0.5$ are rejected. This requirement reduces the contribution from the background due to the reaction $\rm e^+e^- \to Z\gamma^* \to \nu\bar{\nu}q\bar{q}$.

(A6a) The energy of the most energetic jet should not exceed 35 GeV and the observed mass should not exceed 56 GeV (63 GeV) for two-jet (three-jet) events. These requirements strongly reduce the remaining background from W^+W^- and $We\nu$ production, since their observed mass peaks at 80 GeV (see Fig. 2).

Events with four or more jets are selected in the second part. Events with a clear four-jet signature are selected by requiring the fourth-most energetic jet to have an energy exceeding 8 GeV and that each jet contains at least one charged particle. These events are rejected if they change from being three-jet to four-jet events at $y_{\rm cut} = y_{34}$ smaller than 0.01, or if they change from being four-jet to five-jet events at a y_{45} value larger than 0.0015.

(A5b) Events are required to have either a clear four-jet signature (as defined above) or no jet with energy exceeding 20 GeV.

No events in the data survive the cuts described above. This is consistent with the expected background from Standard Model processes of 0.24 events. The numbers of events remaining after each cut are listed in Table 2. After cut (A1), which rejects multihadronic $\gamma\gamma$ events, there is good agreement between the data and the Standard Model predictions.

For events falling into category (A) the efficiencies for $\tilde{\chi}_1^+\tilde{\chi}_1^-$ events are listed in Table 3 for the $\tilde{\chi}_1^0 W^{*\pm}$ decay of the $\tilde{\chi}_1^\pm$. The numbers for $\Delta M_+ \leq 5$ GeV suffer from large statistical fluctuations but these do not matter for the final results as very few events fall into category (A) when ΔM_+ is small.

4.1.2 Analysis B ($N_{\rm ch} > 4$ with isolated leptons)

In $\tilde{\chi}_1^+\tilde{\chi}_1^-$ events in which one of the $\tilde{\chi}_1^\pm$ decays leptonically, the events tend to fall into category (B). The fraction of $\tilde{\chi}_1^+\tilde{\chi}_1^-$ events falling into category (B) is 32–61% if ΔM_+ is at least 5 GeV.

To reduce the background from $e^+e^- \to Z\gamma$ events and events from two-photon processes the following cuts are applied:

(B1) The visible energy in the region $|\cos\theta| > 0.9$ should be less than 20% of the total visible energy. The polar angle of the missing momentum direction, $\theta_{\rm miss}$, is required to satisfy $|\cos\theta_{\rm miss}| < 0.9$. The polar angle of the thrust axis direction, $\theta_{\rm thrust}$, is also required to satisfy $|\cos\theta_{\rm thrust}| < 0.9$.

(B2) P_t and $P_t^{\rm HCAL}$ should be greater than 5 GeV and 6 GeV, respectively. The distribution of $P_t^{\rm HCAL}$ is shown in Fig. 3 after cut (B1).

(B3) The acoplanarity angle as defined in cut (A3) is required to be greater than 20°.

To reduce the contribution of events from W boson production the following three cuts are applied.

(B4) The invariant mass of the event excluding the highest energy lepton, $M_{\rm rest}$, should be smaller than 65 GeV.

	data	total bkg.	$q\bar{q}(\gamma)$	$\ell^+\ell^-(\gamma)$	'$\gamma\gamma$'	4-f	$\tilde{\chi}_1^+\tilde{\chi}_1^-$	$\tilde{\chi}_1^+\tilde{\chi}_1^-$
$m_{\tilde{\chi}_1^\pm}$ (GeV)							80	80
$m_{\tilde{\chi}_1^0}$ (GeV)							60	20
cut								
no cuts	–	–	–	–	–	–	1000	1000
Presel.+(A)	1448	1282.	777.	13.7	408.	83.0	280	491
Cut (A1)	423	407.	267.	2.54	80.9	56.4	224	375
Cut (A2)	193	196.	156.	1.73	0.72	37.7	217	339
Cut (A3)	8	4.50	0.15	0.01	0.22	4.11	197	216
Cut (A4)	7	3.84	0.15	0.01	0.22	3.45	197	192
	Events with two or three jets							
2 or 3 jets	5	2.94	0.08	0.01	0.08	2.76	121	107
Cut (A5a)	4	2.75	0.08	0.007	0.08	2.57	116	103
Cut (A6a)	0	0.18	0.00	0.002	0.08	0.09	50	36
	Events with at least four jets							
≥ 4 jets	1	0.65	0.07	0.00	0.00	0.58	75	85
Cut (A5b)	0	0.06	0.006	0.00	0.00	0.06	65	51
	Final Counts							
Net	0	0.24	0.006	0.002	0.08	0.15	115	87

Table 2: The remaining numbers of events after each cut for various background processes normalized to 10.3 pb^{-1} are compared with data for category (A). Numbers for two simulated event samples of $\tilde{\chi}_1^+\tilde{\chi}_1^-$ with $\tilde{\chi}_1^+ \to \tilde{\chi}_1^0\mathrm{W}^*$ are also given.

$m_{\tilde{\chi}_1^+}$ (GeV)	50	55	60	65	70	75	80	85
ΔM_+								
3.0 GeV	7	12	6	12	0	2	0	0
5.0 GeV	16	29	27	28	15	23	7	28
10.0 GeV	47	50	47	48	51	45	53	51
20.0 GeV	28	33	35	43	49	54	58	58
$m_{\tilde{\chi}_1^+}/2$	19	19	16	24	23	25	26	22
$m_{\tilde{\chi}_1^+} - 20$ GeV	15	14	13	13	15	14	16	13
$m_{\tilde{\chi}_1^+} - 10$ GeV	11	10	11	9	8	9	6	6
$m_{\tilde{\chi}_1^+}$	8	5	6	5	5	5	3	0

Table 3: The detection efficiencies for events falling into category (A), in percent, for $\tilde{\chi}_1^+\tilde{\chi}_1^-$ with two $\tilde{\chi}_1^\pm \to \tilde{\chi}_1^0\mathrm{W}^{*\pm}$ decays normalized to the number of events without isolated leptons and with $N_{\mathrm{ch}} > 4$.

(B5) Events are rejected if the reconstructed highest lepton energy, $E_\ell^{\max}$, exceeds 30 GeV. The scatter plots of $M_{\rm rest}$ vs. $E_\ell^{\max}$ after cut (B3) are shown in Fig. 4.

(B6) The invariant mass of the event is required to be smaller than 75 GeV to reduce contributions from W^+W^- and Weν processes. This cut suppresses W-pair events which decay to $\ell\nu q\bar{q}'g$, in which the charged lepton escapes down the beampipe and a hadronic jet from the $q\bar{q}'g$ system is misidentified as a tau lepton; these are not removed by cuts (B4) or (B5).

The numbers of events remaining after each cut are shown in Table 4 for the OPAL data, the Monte Carlo simulations of the various background sources and for three samples of simulated $\tilde{\chi}_1^+\tilde{\chi}_1^-$ events. There are no events passing all selection cuts, while the expected background is 0.29 events. For events falling into category (B) the efficiencies for $\tilde{\chi}_1^+\tilde{\chi}_1^-$ events are listed in Table 5 for the $\tilde{\chi}_1^0 W^{*\pm}$ decay of the $\tilde{\chi}_1^\pm$.

4.1.3 Analysis C ($N_{\rm ch} \leq 4$)

Events in which both charginos decay hadronically, but with small ΔM_+, and events in which both charginos decay leptonically tend to fall into category (C). The fraction of $\tilde{\chi}_1^+\tilde{\chi}_1^-$ events falling into category (C) is 9–32% for $\Delta M_+ \geq 10$ GeV and $\geq 55\%$ for $\Delta M_+ \leq 5$ GeV. This analysis will also be used in the neutralino search as described later.

Events are forced into two jets using the Durham jet algorithm [29] and are required to satisfy the following cuts on the jet and event variables:

(C1) One of the jets must have a transverse momentum greater than 1.5 GeV and the other must have a transverse momentum greater than 1.0 GeV.

(C2) A cut is applied to P_t (shown in Fig. 5) at a value that depends on the acoplanarity angle. The separation by acoplanarity angle is needed to reduce efficiently the background from

	data	total	$q\bar{q}(\gamma)$	$\ell^+\ell^-(\gamma)$	'$\gamma\gamma$'	4-f	$\tilde{\chi}_1^+\tilde{\chi}_1^-$		
$m_{\tilde{\chi}_1^\pm}$ (GeV)							80	80	80
$m_{\tilde{\chi}_1^0}$ (GeV)							70	40	20
cut									
no cuts							1000	1000	1000
Presel.+(B)	1296	1027.	18.9	24.9	939.	44.0	518	378	329
Cut (B1)	213	196.	3.81	5.86	155.	30.9	430	296	269
Cut (B2)	36	37.3	2.48	4.27	0.53	30.0	323	286	264
Cut (B3)	14	17.4	0.07	0.12	0.00	17.2	308	241	223
Cut (B4)	1	3.77	0.04	0.08	0.00	3.65	308	220	168
Cut (B5)	0	0.45	0.01	0.04	0.00	0.40	308	214	163
Cut (B6)	0	0.29	0.01	0.03	0.00	0.25	308	208	154

Table 4: The remaining numbers of events for data and for various background processes normalized to 10.3 pb^{-1} are compared after each cut in category (B). Numbers for three simulated event samples of $\tilde{\chi}_1^+\tilde{\chi}_1^-$ with $\tilde{\chi}_1^+ \to \tilde{\chi}_1^0 W^*$ are also given.

$m_{\tilde{\chi}_1^+}$ (GeV)	50	55	60	65	70	75	80	85
ΔM_+								
3.0 GeV	2	6	3	2	2	2	0	0
5.0 GeV	22	27	25	21	18	20	19	22
10 GeV	43	47	54	54	53	55	56	58
20 GeV	49	55	58	61	56	61	69	63
$m_{\tilde{\chi}_1^+}/2$	51	50	48	53	52	52	53	60
$m_{\tilde{\chi}_1^+} - 20$ GeV	42	41	42	42	45	41	44	41
$m_{\tilde{\chi}_1^+} - 10$ GeV	34	41	35	34	35	32	27	23
$m_{\tilde{\chi}_1^+}$	33	31	30	27	19	19	11	2

Table 5: The detection efficiencies in percent for $\tilde{\chi}_1^+\tilde{\chi}_1^-$ with two $\tilde{\chi}_1^\pm \to \tilde{\chi}_1^0 \mathrm{W}^{*\pm}$ decays normalized to the number of events in category (B).

tau pairs that occurs at low acoplanarity angles. To reject these events, which tend to be back-to-back, a cut on the component of P_t transverse to the thrust axis, a_t, is applied if the acoplanarity angle is small. Even when P_t is large, a_t is relatively small for tau pairs as compared to the signals. For events with ϕ_{acop} <50° it is required that $|\cos\theta_a^{\mathrm{miss}}|$ be less than 0.95 (where $\theta_a^{\mathrm{miss}} = \tan^{-1}(a_t/P_z)$ and P_z is the longitudinal component of the missing momentum), P_t/E_{beam} be greater than 0.035, and that a_t/E_{beam} exceed 0.025. For events with ϕ_{acop} >50° it is required that $|\cos\theta_{\mathrm{miss}}|$ be less than 0.90, and that P_t/E_{beam} exceed 0.050.

(C3) To reduce the $\mathrm{e^+e^-}\mu^+\mu^-$ background, events are rejected if there is evidence in the muon chambers, hadron calorimeter strips or central detector of a muon escaping in the very forward region, back to back (within 1 rad) with the direction of the momentum sum of the dijet system. Also, events are rejected if there is a relatively large fraction of hadronic energy ($E_{\mathrm{HCAL}} > 0.05E_{\mathrm{tracks}}$) in the event, where E_{tracks} is the sum of the energy of the good tracks and E_{HCAL} is the sum of the energy in the hadron calorimeter clusters. Lastly the events must be electrically neutral and neither jet may have a charge of magnitude exceeding 1.

(C4) The two-photon background is further reduced by rejecting events if either of the jets has $|\cos\theta| > 0.75$.

(C5) The acoplanarity angle is required to be greater than 30°. This removes much of the $\ell^+\ell^-\gamma$ background.

(C6) To remove the W-pair background, events are rejected if one of the jets has an energy greater than 22 GeV. The distributions of the energy of the higher energy jet are shown in Fig. 6 after all other cuts.

The total background predicted by the Standard Model is 0.34 events for 10.3 pb^{-1}. The numbers of events passing each cut are given in Table 6 for data, background and two simulated signal samples. For events falling into category (C) the efficiencies for $\tilde{\chi}_1^+\tilde{\chi}_1^-$ events are listed in Table 7 for the $\tilde{\chi}_1^0\mathrm{W}^{*\pm}$ decay of the $\tilde{\chi}_1^\pm$. No data events survive the category (C) cuts.

	data	total bkg.	$q\bar{q}(\gamma)$	$\ell^+\ell^-(\gamma)$	'$\gamma\gamma$'	4-f	$\tilde{\chi}_1^+\tilde{\chi}_1^-$	$\tilde{\chi}_1^0\tilde{\chi}_2^0$
$m_{\tilde{\chi}_1^\pm}$ (GeV)							70	–
$m_{\tilde{\chi}_1^0}$ (GeV)							65	60
$m_{\tilde{\chi}_2^0}$ (GeV)							–	70
cut								
no cuts	–	–	–	–	–	–	1000	1000
Presel.+(C)	3566	3195.	0.512	2004.	1173.	17.9	397	341
Cut (C1)	2335	2204.	0.332	1759.	429.	15.8	286	234
Cut (C2)	16	18.0	0.01	5.77	2.24	9.97	158	175
Cut (C3)	8	10.1	0.01	3.16	0.70	6.20	106	118
Cut (C4)	4	6.65	0.00	2.27	0.26	4.12	79	83
Cut (C5)	1	3.58	0.00	0.15	0.25	3.18	74	83
Cut (C6)	0	0.34	0.00	0.006	0.25	0.08	74	83

Table 6: For category (C), which is used in the searches for both charginos and neutralinos, the remaining numbers of events after each cut are compared with various background processes normalized to 10.3 pb^{-1}. Numbers for simulated event samples of $\tilde{\chi}_1^+\tilde{\chi}_1^-$ with $\tilde{\chi}_1^+ \to \tilde{\chi}_1^0 W^*$ and $\tilde{\chi}_1^0\tilde{\chi}_2^0$ with $\tilde{\chi}_2^0 \to \tilde{\chi}_1^0 Z^*$ are also given.

$m_{\tilde{\chi}_1^+}$ (GeV)	50	55	60	65	70	75	80	85
ΔM_+								
3.0 GeV	5	5	4	6	4	2	3	2
5.0 GeV	11	13	11	11	13	11	9	13
10.0 GeV	12	15	14	17	14	16	20	18
20.0 GeV	9	13	7	10	13	15	20	18
$m_{\tilde{\chi}_1^+}/2$	7	8	11	6	7	9	13	8
$m_{\tilde{\chi}_1^+} - 20$ GeV	4	6	8	10	9	5	5	1
$m_{\tilde{\chi}_1^+} - 10$ GeV	2	8	2	4	4	4	4	2
$m_{\tilde{\chi}_1^+}$	2	6	9	3	3	3	2	3

Table 7: The detection efficiencies in percent for $\tilde{\chi}_1^+\tilde{\chi}_1^-$ with $\tilde{\chi}_1^\pm \to \tilde{\chi}_1^0 W^{*\pm}$ decay normalized to the number of category (C) events.

4.1.4 Combined efficiencies and backgrounds for $\tilde{\chi}_1^+\tilde{\chi}_1^-$

The overall efficiency for each mass pair combination is obtained by taking the sum of the efficiencies for categories (A), (B) and (C) weighted by the fraction of signal events falling into each category. Overall efficiencies for $\tilde{\chi}_1^+\tilde{\chi}_1^-$ events are given in Table 8. As shown in this table, the efficiencies are 29–57% if the mass difference between $\tilde{\chi}_1^\pm$ and $\tilde{\chi}_1^0$ is ≥ 10 GeV and $\leq m_{\tilde{\chi}_1^\pm}/2$. The efficiency at an arbitrary point of $m_{\tilde{\chi}_1^+}$ and $m_{\tilde{\chi}_1^0}$ is obtained by interpolation using a polynomial fit to the efficiencies determined from the Monte Carlo. The total background expected for this search is the sum of the background contributions from each category. The total background expected for 10.3 pb^{-1} is 0.87 events, consistent with no events being observed in the data after all cuts.

$m_{\tilde{\chi}_1^+}$ (GeV)	50	55	60	65	70	75	80	85
ΔM_+								
3.0 GeV	5	5	4	6	4	2	2	1
5.0 GeV	15	19	17	16	15	15	12	17
10 GeV	36	39	41	43	41	42	44	46
20 GeV	35	40	41	47	46	51	57	53
$m_{\tilde{\chi}_1^+}/2$	31	32	29	33	33	34	35	35
$m_{\tilde{\chi}_1^+} - 20$ GeV	24	24	25	24	25	23	25	22
$m_{\tilde{\chi}_1^+} - 10$ GeV	19	23	19	17	18	17	13	11
$m_{\tilde{\chi}_1^+}$	16	15	15	13	10	10	6	1

Table 8: The detection efficiencies in percent combined for the three categories for $\tilde{\chi}_1^+\tilde{\chi}_1^-$ followed by the decay $\tilde{\chi}_1^\pm \to \tilde{\chi}_1^0 \mathrm{W}^{*\pm}$.

4.2 Detection of neutralinos

The search for neutralinos is performed by dividing the event sample into two categories:

(C) $N_{\mathrm{ch}} \leq 4$.

(D) $N_{\mathrm{ch}} > 4$.

Events falling into category (D) have a monojet topology and the cuts provide better performance for $\tilde{\chi}_1^0\tilde{\chi}_2^0$ detection than would have been obtained using the cuts of categories (A) and (B). For events with $N_{\mathrm{ch}} \leq 4$ the category (C) cuts, as described in 4.1.3, are used.

The fractions of simulated $\tilde{\chi}_1^0\tilde{\chi}_2^0$ events falling into each of the two categories for $\tilde{\chi}_2^0 \to \tilde{\chi}_1^0 \mathrm{Z}^{(*)}$ decay are shown in Table 9. The fraction of events falling into category (C) is 28–42% for $\Delta M_0 \geq 20$ GeV but increases to above 85% when $\Delta M_0 \leq 5$ GeV. The efficiencies for $\tilde{\chi}_1^0\tilde{\chi}_2^0$ events for the $\tilde{\chi}_1^0\mathrm{Z}^*$ decay of $\tilde{\chi}_2^0$, normalized to $\tilde{\chi}_1^0\tilde{\chi}_2^0 \to \tilde{\chi}_1^0\mathrm{Z}^*$ ($\mathrm{Z}^* \to \mathrm{q\bar{q}}, \ell^+\ell^-$), are listed in Table 10. In category (C) 20% (absolute fraction) of the events are invisible due to $\tilde{\chi}_2^0 \to \tilde{\chi}_1^0 \mathrm{Z}^{(*)} \to \tilde{\chi}_1^0 \nu\bar{\nu}$ decays.

$\tilde{\chi}^0_2\tilde{\chi}^0_1$	$(m_{\tilde{\chi}^0_2} + m_{\tilde{\chi}^0_1})$ GeV	100	110	120	130	140	150	160	170
ΔM_0	Category								
3.0 GeV	(C)	98	98	99	98	99	99	99	99
	(D)	2	2	1	2	1	1	1	1
5.0 GeV	(C)	86	85	88	87	87	89	88	89
	(D)	14	15	12	13	13	11	12	11
10 GeV	(C)	60	62	59	62	58	60	58	59
	(D)	40	38	41	38	42	40	42	41
20 GeV	(C)	41	42	40	39	39	38	40	40
	(D)	59	58	60	61	61	62	60	60
30 GeV	(C)	34	–	34	–	35	–	34	–
	(D)	66	–	66	–	65	–	66	–
50 GeV	(C)	–	30	–	33	–	30	–	31
	(D)	–	70	–	67	–	70	–	69
70 GeV	(C)	30	–	30	–	31	–	31	–
	(D)	70	–	70	–	69	–	69	–
80 GeV	(C)	30	31	30	30	31	30	30	30
	(D)	70	69	70	70	69	70	70	70
90 GeV	(C)	–	28	–	30	–	29	–	30
	(D)	–	72	–	70	–	71	–	70
110 GeV	(C)	–	–	28	–	31	–	29	–
	(D)	–	–	72	–	69	–	71	–
130 GeV	(C)	–	–	–	–	–	30	–	31
	(D)	–	–	–	–	–	70	–	69
150 GeV	(C)	–	–	–	–	–	–	30	–
	(D)	–	–	–	–	–	–	70	–

Table 9: The percentages of the simulated $\tilde{\chi}^0_1\tilde{\chi}^0_2$ event samples falling into each of the two categories for $\tilde{\chi}^0_2 \to \tilde{\chi}^0_1 \mathrm{Z}^{(*)}$ decay, where $\Delta M_0 = m_{\tilde{\chi}^0_2} - m_{\tilde{\chi}^0_1}$. In category (C) 20% (absolute fraction) of the events are invisible events due to $\tilde{\chi}^0_2 \to \tilde{\chi}^0_1 \mathrm{Z}^{(*)} \to \tilde{\chi}^0_1 \nu\bar{\nu}$ decays.

4.2.1 Analysis D ($\mathbf{N_{ch} > 4}$ Neutralino selection)

In $\tilde{\chi}^0_1\tilde{\chi}^0_{2,3}$ events, if the $\tilde{\chi}^0_{2,3}$ decays hadronically, the events tend to fall into category (D). Events have to satisfy the following cuts:

To reduce the background from $\mathrm{e^+e^-} \to \mathrm{Z}\gamma$ and two-photon processes the following cuts are applied.

(D1) The visible energy in the region $|\cos\theta| > 0.9$ should be less than 15% of the total visible energy. The polar angle of the missing momentum direction θ_{miss} is required to satisfy $|\cos\theta_{\mathrm{miss}}| < 0.9$.

(D2) P_t and P_t^{HCAL} should be greater than 5 GeV and 6 GeV, respectively.

(D3) The acoplanarity angle as defined in cut (A3) is required to be greater than 15°. Both jets should have a polar angle in the range $|\cos\theta| < 0.95$. Figure 7 shows the distribution of ϕ_{acop} for the various background processes and signal samples after cut (D2).

$(m_{\tilde{\chi}_2^0} + m_{\tilde{\chi}_1^0})$ (GeV)	100	110	120	130	140	150	160	170
ΔM_0								
3.0 GeV	1	1	0	0	0	0	0	0
5.0 GeV	8	7	6	5	4	3	1	1
10.0 GeV	13	14	16	16	14	14	14	16
20.0 GeV	12	13	16	18	15	16	17	18
30.0 GeV	6	–	9	–	14	–	23	–
50.0 GeV	–	3	–	5	–	8	–	6
70.0 GeV	2	–	2	–	2	–	1	–
90.0 GeV	–	0	–	0	–	2	–	0
110.0 GeV		–	2	–	1	–	1	–
130.0 GeV				–	–	1	–	0
150.0 GeV						–	0	–

Table 10: The detection efficiencies in percent for $\tilde{\chi}_1^0\tilde{\chi}_2^0$ with $\tilde{\chi}_2^0 \to \tilde{\chi}_1^0 \mathrm{Z}^*$ decay (with $\mathrm{Z}^* \to \ell^+\ell^-$ or $\mathrm{Z}^* \to \mathrm{q\bar{q}}$) normalized to the number of category (C) events excluding the $\tilde{\chi}_2^0 \to \tilde{\chi}_1^0\nu\nu$ invisible events.

After these cuts, the remaining background events come predominantly from $\mathrm{Z}\gamma^*(\to \nu\bar{\nu}\mathrm{q\bar{q}})$, $\mathrm{W^+W^-}(\to \ell\nu\mathrm{q\bar{q}}')$ and $\mathrm{We}\nu(\to \mathrm{q\bar{q}}'\mathrm{e}\nu)$. If the invariant mass of the event is smaller than 20 GeV, the following cut is applied to reduce the contribution of events from the $\mathrm{Z}\gamma^* \to \nu\bar{\nu}\mathrm{q\bar{q}}$ process:

(D4) The ratio of visible mass to visible energy, $M_{\mathrm{vis}}/E_{\mathrm{vis}}$, is required to be larger than 0.4.

If the visible mass is greater than 20 GeV, the following four cuts are applied to reduce the background from the $\mathrm{W^+W^-}$ and $\mathrm{We}\nu$ processes:

(D5.1) To keep high efficiency for all lepton flavours, a simple inclusive leptonic jet identification is used. Events are forced to be reconstructed into three jets. The lowest charged multiplicity, N_{min}, jet is defined as a 'leptonic jet', and the other two jets as 'hadronic jets'. If there is more than one jet with charged multiplicity equal to N_{min}, then the low multiplicity jet with the largest energy is defined as the leptonic jet. The energy of the leptonic jet, E_{lep}, and the invariant mass of the two hadronic jets, M_{had}, are required to satisfy $(M_{\mathrm{had}} + 2.2 \times E_{\mathrm{lep}}) \leq 110$ GeV. Figure 8 shows the scatter plot of M_{had} versus E_{lep} just before cut (D5.1).

(D5.2) If part of the jet escapes undetected down the beampipe in a $\mathrm{W^+W^-} \to \tau\nu\mathrm{q\bar{q}}$ event, the event will have small visible hadronic mass and survive cut D5.1. To eliminate such events, the condition $y_{23}E_{\mathrm{vis}}^2 < 40$ GeV^2 is imposed.

(D5.3) Since the topology of the signal events is very similar to that for $\mathrm{We}\nu$ events, it is very difficult to separate the signal from background by global kinematical cuts. Using the decay length method, a loose b-tagging [35] is applied when M_{vis} is larger than 60 GeV to reduce the contribution of events from the $\mathrm{We}\nu$ background process and retain some efficiency for $\tilde{\chi}_2^0 \to \tilde{\chi}_1^0\mathrm{b\bar{b}}$ decays. The systematic errors of the b-tagging are mainly due to well understood uncertainties in the decay length resolution and in the b-lifetime. This

selection allows limits to be set in the small region of large $m_{\tilde{\chi}^0_2}$ and low $m_{\tilde{\chi}^0_1}$ that is not accessible within the framework of the MSSM.

(D5.4) The acoplanarity angle determined as described for cut (A3) is required to be greater than 20°, if the number of reconstructed jets, obtained using the Durham algorithm with $y_{\rm cut} = 0.005$, is larger than or equal to three. This cut reduces potentially mismeasured three-jet events.

The numbers of events remaining after each cut are listed in Table 11. The efficiencies for $\tilde{\chi}^0_2\tilde{\chi}^0_1$ events falling into category (D) are listed in Table 12.

4.2.2 Combined efficiencies and backgrounds for $\tilde{\chi}^0_1\tilde{\chi}^0_2$

The net efficiency for each mass pair combination is obtained by taking the sum of the efficiencies for categories (C) and (D) weighted by the fraction of signal events falling into each category. Overall efficiencies for $\tilde{\chi}^0_2\tilde{\chi}^0_1$ events are given in Table 13. As shown in this table, the efficiencies are 29–43% if $\Delta M_0 \geq 20$ GeV and ≤ 70 GeV. The total background expected for this search, which is the sum of the background contributions from categories (C) and (D), is 0.96 events.

	data	total	$q\bar{q}(\gamma)$	$\ell^+\ell^-(\gamma)$	'$\gamma\gamma$'	4-f	$\tilde{\chi}^0_1\tilde{\chi}^0_2$		
$m_{\tilde{\chi}^0_2} + m_{\tilde{\chi}^0_1}$							160GeV		
$m_{\tilde{\chi}^0_2} - m_{\tilde{\chi}^0_1}$ (GeV)							10	30	70
no cuts							1000	1000	1000
Presel.+(D)	2744	2309.	796.	38.6	1347.	127	476	801	816
Cut (D1)	642	608.	270.	8.36	243.	86.7	417	659	664
Cut (D2)	238	240.	164.	6.14	1.25	68.8	192	622	652
Cut (D3)	35	35.9	3.89	0.22	0.30	31.5	188	577	553
$M_{\rm vis} \leq$20 GeV	2	0.65	0.00	0.006	0.22	0.43	188	312	25
Cut (D4)	0	0.15	0.00	0.002	0.08	0.06	163	234	5
$M_{\rm vis} >$20 GeV	33	35.3	3.89	0.21	0.08	31.1	0	265	528
Cut (D5.1)	5	4.45	0.14	0.05	0.08	4.17	0	265	522
Cut (D5.2)	3	1.66	0.02	0.02	0.08	1.54	0	259	514
Cut (D5.3)	0	0.56	0.02	0.01	0.08	0.44	0	259	392
Cut (D5.4)	0	0.47	0.02	0.01	0.00	0.44	0	248	390
Net	0	0.62	0.02	0.02	0.08	0.50	163	482	395

Table 11: The remaining numbers of events for the various background processes normalized to 10.3 $\rm pb^{-1}$ after each cut in category (D). Numbers for three simulated event samples of $\tilde{\chi}^0_1\tilde{\chi}^0_2$ with $\tilde{\chi}^0_2 \to \tilde{\chi}^0_1\ell^+\ell^-$ or $\tilde{\chi}^0_1 q\bar{q}$ are also given.

$m_{\tilde{\chi}_2^0} + m_{\tilde{\chi}_1^0}$(GeV)	100	110	120	130	140	150	160	170
ΔM_0								
3.0 GeV	10	10	0	4	0	0	0	0
5.0 GeV	21	16	14	9	5	4	3	0
10 GeV	37	38	40	37	40	40	31	33
20 GeV	47	52	53	50	58	57	59	60
30 GeV	51	–	55	–	57	–	58	–
50 GeV	–	55	–	61	–	61	–	57
70 GeV	45	–	42	–	43	–	46	–
80 GeV	34	30	31	32	30	28	30	32
90 GeV	–	18	–	15	–	11	–	11
110 GeV		–	8	–	9	–	8	–
130 GeV				–	–	6	–	7
150 GeV						–	7	–

Table 12: The detection efficiencies in percent for $\tilde{\chi}_1^0\tilde{\chi}_2^0$ with $\tilde{\chi}_2^0 \to \tilde{\chi}_1^0 \mathrm{Z}^{(*)}$ normalized to the number of events in category (D).

$m_{\tilde{\chi}_2^0} + m_{\tilde{\chi}_1^0}$(GeV)	100	110	120	130	140	150	160	170
ΔM_0								
3.0 GeV	1	1	0	0	0	0	0	0
5.0 GeV	8	7	6	5	3	3	1	1
10 GeV	20	20	23	21	22	22	18	20
20 GeV	31	33	35	34	38	38	39	40
30 GeV	34	–	38	–	39	–	42	–
50 GeV	–	39	–	41	–	43	–	40
70 GeV	32	–	29	–	30	–	32	–
80 GeV	24	21	22	22	20	20	21	22
90 GeV	–	13	–	11	–	8	–	7
110 GeV		–	6	–	6	–	6	–
130 GeV				–	–	4	–	5
150 GeV						–	4	–

Table 13: The detection efficiencies in percent for $\tilde{\chi}_1^0\tilde{\chi}_2^0$ with $\tilde{\chi}_2^0 \to \tilde{\chi}_1^0 \mathrm{Z}^*$ decay for category (C) and (D) combined. The invisible decay $\tilde{\chi}_2^0 \to \tilde{\chi}_1^0 \nu\bar{\nu}$ which could occur 20% of the time is assumed to be undetectable.

4.3 Detection of chargino events with WW-like signature

A special analysis for the chargino search was performed for the case in which the chargino mass is close to the W mass and the light neutralinos are almost massless. The event topology of such chargino pair events is similar to that of ordinary $\mathrm{W}^+\mathrm{W}^-$ events but with somewhat larger missing energy as the neutralinos tend to have small but significant momentum. If $\tan\beta \approx 1$ and $M_2 \approx \mu \approx 0$, the chargino and light neutralinos satisfy these conditions as described in Section 1.

This analysis may be sensitive to the details of the energy flow, especially in the $e^+e^- \to W^+W^-$ background simulation, as will become apparent in cuts (E4) and (F5) in the selections that are presented in the following. Therefore the observed energies in the simulated events are scaled with the ratio of the centre-of-mass energies of the data and the simulated events, when calculating efficiencies of background events at each energy (170.3 GeV and 172.3 GeV).

The search for such chargino events is performed by dividing the event sample into two categories described as follows:

4.3.1 Analysis E ($N_{\rm ch} > 4$ and no isolated leptons)

When both charginos decay into $\tilde{\chi}^0_i q\bar{q}'$ ($i = 1, 2$), the event shape is similar to that of the W^+W^- events in which both W's decay hadronically. For events with more than four charged tracks ($N_{\rm ch} > 4$) and with no isolated leptons (category (A)) the following cuts are applied:

(E1) The visible energy in the region defined by $|\cos\theta| > 0.9$ should be less than 20% of the total visible energy. In addition, to reduce background from two-photon processes $|\cos\theta_{\rm miss}|$ should be smaller than 0.9.

(E2) The magnitude of the momentum component longitudinal to the beam axis should be smaller than 25 GeV. This cut reduces the background from $\ell\ell q\bar{q}$ final states.

(E3) The maximum EM cluster energy should be smaller than 35 GeV.

The above three cuts reject $Z\gamma$ events with a hadronic Z decay. Since the signal events have missing energy and missing momentum due to the invisible neutralinos, the following cut is applied to reduce the background from W-pair events.

(E4) The visible energy should be between 50 and 150 GeV. The distribution of the visible energy is shown in Fig. 9 after cut (E3).

The following two cuts are applied to reduce the contribution from $e^+e^- \to q\bar{q}$ events.

(E5) The number of jets reconstructed with the Durham algorithm using a jet resolution parameter of $y_{\rm cut} = 0.005$ should be at least four.

(E6) The sum of the two highest jet energies ($E_1 + E_2$) should be smaller than 100 GeV.

In Table 14, the remaining numbers of simulated events for background processes and for three samples of simulated $\tilde{\chi}^+_1\tilde{\chi}^-_1$ events are given.

The main background comes from four-fermion processes as well as $q\bar{q}(\gamma)$ events. Seven events are observed which is consistent with the total expected background of 7.0 events. The net detection efficiency for chargino events is typically 18–20% for an 80 GeV chargino decaying into a light stable neutralino ($m_{\tilde{\chi}^0_1} < 10$ GeV). The efficiency does not drop by more than 1% when both charginos decay into $W^{(*)}\tilde{\chi}^0_2$ and $\tilde{\chi}^0_2$ decays into $\tilde{\chi}^0_1\gamma$.

	data	total	$q\bar{q}(\gamma)$	$\ell^+\ell^-(\gamma)$	'$\gamma\gamma$'	4-f	$\tilde{\chi}_1^+\tilde{\chi}_1^-$		
$m_{\tilde{\chi}_1^\pm}$ (GeV)							80	80	80
$m_{\tilde{\chi}_1^0}$ (GeV)							0	0	10
$m_{\tilde{\chi}_2^0}$ (GeV)							–	2	–
no cuts							1000	1000	1000
Presel.+(E)	1448	1282.	777.	13.7	408.	83.0	522	510	499
Cut (E1)	450	429.	271.	2.54	96.1	59.0	412	410	400
Cut (E2)	418	408.	255.	2.11	96.0	54.7	356	365	326
Cut (E3)	281	270.	123.	0.63	96.0	50.3	348	355	320
Cut (E4)	39	41.8	28.4	0.47	0.59	12.3	292	258	310
Cut (E5)	7	7.96	3.22	0.000	0.08	4.66	200	194	184
Cut (E6)	7	7.00	2.44	0.000	0.08	4.47	199	186	183

Table 14: The remaining numbers of events for the various background processes normalized to 1.0 and 9.3 pb^{-1} for $\sqrt{s} = 170.3$ and 172.3 GeV, respectively, are compared after each cut in category (E). Numbers for three simulated event samples of $\tilde{\chi}_1^+\tilde{\chi}_1^-$ with $\tilde{\chi}_1^+ \to (\tilde{\chi}_1^0$ or $\tilde{\chi}_2^0)\mathrm{W}^*$ are also given (starting from 1000 events).

4.3.2 Analysis F ($N_{\mathrm{ch}} > 4$ with isolated leptons)

When one of the charginos decays into $\tilde{\chi}_i^0 q\bar{q}'$ $(i = 1, 2)$ and the other into $\tilde{\chi}_j^0 \ell\nu$ $(j = 1, 2)$, the event shape is similar to that of $\mathrm{W}^+\mathrm{W}^- \to \nu\ell q\bar{q}'$ events. Events with more than four charged tracks ($N_{\mathrm{ch}} > 4$) and at least one isolated lepton (category (B)) are selected and the following cuts are applied:

(F1) To reduce the contribution of events from two-photon processes and $\mathrm{Z}\gamma$ events where the γ escaped undetected down the beam pipe, $|\cos\theta_{\mathrm{miss}}|$ should be smaller than 0.9.

(F2) To reduce the background from two-photon processes, P_t and P_t^{HCAL} were required to be greater than 10 GeV.

(F3) The visible energy should be smaller than 125 GeV. This cut is effective in rejecting the well contained $\mathrm{e}^+\mathrm{e}^- \to q\bar{q}$ and W pair events.

(F4) The isolated lepton energy should be smaller than 50 GeV.

(F5) The invariant mass of the event excluding the highest momentum isolated lepton should be between 15 and 80 GeV. The M_{rest} distribution is shown in Fig. 10 for the data, the expected background processes and the signal after cut (F4).

In Table 15, the remaining numbers of simulated events for background processes and for three samples of simulated $\tilde{\chi}_1^+\tilde{\chi}_1^-$ events are given.

The main background comes from four-fermion processes. Eight events are observed which is consistent with the total expected background of 10.4 events. The net detection efficiency for chargino events is typically 24% for a 80 GeV chargino decaying into a light stable neutralino ($m_{\tilde{\chi}_1^0} < 10$ GeV). The efficiency drops by about 7% when both charginos decay into $\mathrm{W}^{(*)}\tilde{\chi}_2^0$ and $\tilde{\chi}_2^0$ decays into $\tilde{\chi}_1^0\gamma$.

	data	total	$q\bar{q}(\gamma)$	$\ell^+\ell^-(\gamma)$	'$\gamma\gamma$'	4-f	$\tilde{\chi}_1^+\tilde{\chi}_1^-$		
$m_{\tilde{\chi}_1^\pm}$ (GeV)							80	80	80
$m_{\tilde{\chi}_1^0}$ (GeV)							0	0	10
$m_{\tilde{\chi}_2^0}$ (GeV)							–	2	–
no cuts							1000	1000	1000
Presel.+(F)	1296	1027.	18.9	24.9	939.	44.0	324	312	327
Cut (F1)	642	601.	7.79	10.5	546.	36.3	301	293	294
Cut (F2)	37	39.1	2.28	3.22	0.10	33.5	284	268	281
Cut (F3)	16	16.3	0.30	1.39	0.10	14.5	266	218	274
Cut (F4)	14	15.5	0.30	1.24	0.05	13.9	252	207	268
Cut (F5)	8	10.4	0.22	0.31	0.00	9.83	235	167	238

Table 15: The remaining numbers of events for the various background processes normalized to 1.0 and 9.3 pb^{-1} for $\sqrt{s} = 170.3$ and 172.3 GeV, respectively, are compared after each cut in category (F). Numbers for three simulated event samples of $\tilde{\chi}_1^+\tilde{\chi}_1^-$ with $\tilde{\chi}_1^+ \to (\tilde{\chi}_1^0$ or $\tilde{\chi}_2^0)\mathrm{W}^*$ are also given (starting from 1000 events).

4.3.3 Combined efficiencies and backgrounds for analyses (E) and (F)

The overall efficiency for each mass pair combination is obtained by taking the weighted sum of the efficiencies for categories (E) and (F). Overall efficiencies for $\tilde{\chi}_1^+\tilde{\chi}_1^-$ events are 35–45%. The total number of expected background events is 17.4, while 15 events are observed.

4.4 Systematic errors and corrections

In analyses (A)-(D), systematic errors on the number of expected signal events arise from the following sources: the measurement of the integrated luminosity (0.6%), Monte Carlo statistics in the various signal samples and the interpolation errors of the efficiencies at arbitrary values of $m_{\tilde{\chi}_1^+}$ ($m_{\tilde{\chi}_2^0}$) and $m_{\tilde{\chi}_1^0}$ (2–10%), modelling of the cut variables in the Monte Carlo simulations[7] (2–4%), errors due to fragmentation uncertainties in hadronic decays ($< 2\%$), the matrix elements leading to different decay parameters ($< 5\%$) and effects of detector calibration ($< 1\%$). The effect of possible trigger inefficiencies has been checked and found to be negligible. These systematic errors are considered to be independent and are added in quadrature (7–12%).

In analyses (A)-(D), the systematic errors on the expected number of background events used to obtain the limits (when combining present with previous results) are due to: Monte Carlo statistics in the simulated background events, uncertainties in the amount of two-photon background, estimated by fitting the P_t distributions of simulated two-photon events and the data (30%); and uncertainties in the simulation of the four-fermion processes, which are estimated by taking the difference between the predictions of the grc4f [23] and the EXCALIBUR [25] generators (17% for chargino, 20% for neutralino). The systematic errors due to the modelling of the cut variables in the detector simulation are 12% for the two-photon processes and 4% for the four-fermion processes in the case of the chargino selection. In the neutralino search these

[7]This is estiimated by comparing the efficiencies obtained by shifting each cut variable by the maximal possible shift in the corresponding distribution which still gives agreement between data and Monte Carlo.

errors become 14% and 5%, respectively. For the neutralino selection an additional uncertainty of 11% due to the b-tagging is included. A 100% systematic error is assumed for the number of background events expected for the $q\bar{q}(\gamma)$ and $\ell^+\ell^-(\gamma)$ states. Therefore, the total expected number of background events is estimated for the chargino search to be 0.87 ± 0.19 (0.02 ± 0.02 from $q\bar{q}(\gamma)$, 0.03 ± 0.03 from $\ell^+\ell^-(\gamma)$, 0.34 ± 0.17 from two-photon processes and 0.48 ± 0.09 from four-fermion final states), and for the neutralino search 0.96 ± 0.22 (0.02 ± 0.02 from $q\bar{q}(\gamma)$, 0.02 ± 0.02 from $\ell^+\ell^-(\gamma)$, 0.34 ± 0.18 from two-photon processes and 0.58 ± 0.13 from four-fermion final states).

In analyses (E) and (F), systematic errors on the number of expected signal events arise from the following sources: the measurement of the integrated luminosity (0.6%); four jet selection in analysis E (0.9%); Monte Carlo statistics of the signal samples and interpolation of the efficiencies at arbitrary values of $m_{\tilde{\chi}_i^+}$ and $m_{\tilde{\chi}_j^0}$ (4-5%); preselection (mainly the cut on the energy deposited in the forward calorimeter) ($< 2\%$); fragmentation uncertainties in hadronic decays (2%); and the energy scale (0.6%).

In analyses (E) and (F) the systematic errors on the number of expected four-fermion background events (dominated by W-pair production) come from modelling of the processes (2.4%), estimated by comparing the numbers obtained with the grc4f, EXCALIBUR and PYTHIA [20] generators, calibration of the energy scale (6%), and the beam energy uncertainty (0.3%). The error due to the uncertainty on the W mass [36] is 0.4%. The systematic errors on the number of expected $e^+e^- \to q\bar{q}(\gamma)$ background events is due to the energy scale (7%), and to the modelling of the process (11%), estimated by comparing the numbers obtained with the PYTHIA and HERWIG [22] generators. The error on the modelling of the processes is mainly due to the limited statistics of the selected Monte Carlo events. The combined error for four-fermion events and for $e^+e^- \to q\bar{q}(\gamma)$ events due to preselection (mainly the cut on the energy deposited in the forward calorimeter) is $< 1.6\%$ and the one due to the four jet selection in analysis E is 1.4%. A 100% systematic error was assigned to the number of lepton-pair and two-photon background events. The errors due to the energy scale for four-fermion and for $e^+e^- \to q\bar{q}(\gamma)$ background events were added linearly. All the other errors were added quadratically. The total number of background events was estimated to be 17.45 ± 1.29. The total number of events surviving all cuts was 15.

The rate of events in which the measured energy in the SW, FD or GC calorimeters, due to noise and beam related background, exceeded the thresholds in the preselection is about 2.3% as estimated from random beam crossing events. Since this effect is not modelled in the simulation, this effect is taken into account by scaling the detection efficiencies by this amount. This correction is applied for all the analyses (A)-(F).

The systematic errors on the numbers of expected signal and background events are summarized in Tables 16 and 17 respectively.

	Analyses (A) to (D)	Analyses (E) and (F)
Integrated luminosity	0.6 %	0.6 %
MC statistics	2−10 %	4−5 %
Cut variables	2−4 %	−
Fragmentation	2 %	2 %
Matrix element	5 %	−
Detector calibration	1 %	−
4-jet selection (E)	−	0.9 %
Preselection	−	2 %
Energy scale	−	0.6 %

Table 16: Systematic uncertainties on the numbers of expected signal events.

		4-f	$q\bar{q}$	$\gamma\gamma$	$\ell^+\ell^-$
Chargino search:	Modelling	17 %	−	30 %	−
Analyses (A) to (C)	Cut variables	4 %	−	12 %	−
	others		100 %		100 %
Neutralino search:	Modelling	20 %	−	30 %	−
Analyses (B) and (D)	Cut variables	5 %	−	14 %	−
	b tagging	11 %	−	11 %	−
	others		100 %		100 %
	Modelling	2.4 %	11 %	−	−
	Energy scale	6 %	7 %	−	−
	Beam energy	0.3 %	−	−	−
Analyses (E) and (F)	W mass	0.4 %	−	−	−
	Preselection	1.6 %	1.6 %	−	−
	4-jet selection (E)	1.4 %	1.4 %	−	−
	others			100%	100 %

Table 17: Systematic uncertainties on the numbers of expected background events.

5 Results

5.1 Limits on the $\tilde{\chi}_1^+\tilde{\chi}_1^-$ and $\tilde{\chi}_1^0\tilde{\chi}_2^0$ cross-sections

A model-independent interpretation is formed by calculating the 95% confidence level (C.L.) upper limits on the production cross-sections for $\tilde{\chi}_1^+\tilde{\chi}_1^-$ and $\tilde{\chi}_1^0\tilde{\chi}_2^0$ assuming the specific decay modes $\tilde{\chi}_1^\pm \to \tilde{\chi}_1^0 W^{*\pm}$ and $\tilde{\chi}_2^0 \to \tilde{\chi}_1^0 Z^*$. From the observation of no events at $\sqrt{s} = 170-172$ GeV in analyses (A)-(D), and using the signal detection efficiencies and their uncertainties, exclusion regions are determined using the procedure outlined in [36], and incorporating systematic errors following the method given in [37] by numerical integration, assuming Gaussian errors. To compute the 95% C.L. upper limits, the previous results obtained at $\sqrt{s} = 161$ GeV [3] (including the observed candidates as well as background expectations where kinematically allowed) have been combined with the present results. For the combination of results from different energies it is assumed that the cross-sections are proportional to $\tilde{\beta}/s$, where $\tilde{\beta}$ is the momentum of the final state $\tilde{\chi}_1^+$ or $\tilde{\chi}_2^0$ in the centre-of-mass system normalized to the beam energy.

Contours of the upper limits for the $\tilde{\chi}_1^+\tilde{\chi}_1^-$ cross-sections are shown in Fig. 11 assuming $\tilde{\chi}_1^\pm \to \tilde{\chi}_1^0 \mathrm{W}^{*\pm}$ with 100% branching fraction. Similarly, contours of the upper limit for the $\tilde{\chi}_1^0\tilde{\chi}_2^0$ cross-sections are shown assuming 100% branching fraction for $\tilde{\chi}_2^0 \to \tilde{\chi}_1^0 \mathrm{Z}^*$ (Fig. 12). The Standard Model branching fractions are used for the W^* and Z^* decays, including the invisible decay mode $\mathrm{Z}^* \to \nu\bar{\nu}$ and taking into account phase-space effects for decays into heavy particles (especially $\mathrm{b\bar{b}}$). Although these limits do not depend on the details of the SUSY models considered, a "typical" field content[8] of the gauginos is assumed, leading to particular production angular distributions that are subsequently used in the estimation of detection efficiencies. There are differences in detection efficiencies due to variations in the angular distributions resulting from using different MSSM parameters corresponding to the same mass combination. The variation of the efficiency is observed to be $< 2\%$. Of the parameters examined, those which result in the lowest efficiency are used.

If the cross-section for $\tilde{\chi}_1^+\tilde{\chi}_1^-$ is larger than 3.0 pb and ΔM_+ is larger than 5 GeV, it is possible to exclude at 95% C.L. the $\tilde{\chi}_1^+$ up to the kinematic limit for $\tilde{\chi}_1^+$ decay via W^*. This is achieved by using analyses (A) to (C) in the non-hatched regions of Fig. 11 and using analyses (E) and (F) in the hatched region. Furthermore $\tilde{\chi}_2^0$ masses up to the kinematical boundary of $(m_{\tilde{\chi}_1^0} + m_{\tilde{\chi}_2^0}) < \sqrt{s}$ are excluded at 95% C.L. for $10 \leq \Delta M_0 \leq 80$ GeV, if the cross-section for $\tilde{\chi}_1^0\tilde{\chi}_2^0$ is larger than 2.0 pb.

5.2 Limits in the MSSM parameter space

The results of the above searches can be interpreted within the framework of the constrained MSSM. The phenomenology of the gaugino-higgsino sector of the MSSM is mostly determined by the parameters M_2, μ and $\tan\beta$ defined earlier. In the absence of light sfermions and light SUSY Higgs particles, these three parameters are sufficient to describe the chargino and neutralino sector completely. Within the constrained MSSM (CMSSM), a large value of the common scalar mass, m_0 (e.g., $m_0 = 1$ TeV) leads to heavy sfermions and therefore to a negligible suppression of the cross-section due to interference from t-channel sneutrino exchange, and chargino and neutralino decays would proceed via a virtual W^* or Z^*, respectively. On the other hand, a light m_0 results in low values of the masses of the $\tilde{\nu}$ and $\tilde{\ell}$, thereby enhancing the contribution of the t-channel exchange diagrams that may have destructive interference with s-channel diagrams, thus reducing the cross-section for chargino pair production. Small values of m_0 also tend to enhance the leptonic branching ratio of charginos, often leading to smaller detection efficiencies. For neutralino pair production the t-channel selectron exchange diagram may interfere positively with the s-channel Z boson diagram to enhance this cross-section, but the size of the chargino cross-section almost always remains larger. The results are therefore presented for two cases: $m_0 = 1$ TeV and the smallest value of m_0 that is compatible with current limits on the $\tilde{\nu}$ mass ($m_{\tilde{\nu}_L} > 43$ GeV [36]), and OPAL limits on the $\tilde{\ell}$ mass, particularly right-handed smuon and selectron pair production [38]. This latter "minimum m_0" case gives the lowest $\tilde{\chi}_1^+\tilde{\chi}_1^-$ production cross-section for $\tan\beta = 1.0$ but not necessarily for larger $\tan\beta$ values.

In the region of small M_2 and large μ, the $\tilde{\chi}_1^\pm$ and $\tilde{\chi}_1^0$ would be almost pure gauginos,

[8] These field contents arise from the MSSM parameters necessary to give as close as possible gaugino masses as those being considered with some mixture of $\tilde{\mathrm{W}}^\pm$ and $\tilde{\mathrm{H}}^\pm$ for charginos and $\tilde{\gamma}$, $\tilde{\mathrm{Z}}$, and $\tilde{\mathrm{H}}_j^0$ for neutralinos. When more than one set of parameters lead to the same set of gaugino masses, the set not yet excluded or with more moderate values of $|\mu|$ and M_2 was chosen.

resulting in large $\tilde{\chi}_1^+\tilde{\chi}_1^-$ cross-sections, but small $\tilde{\chi}_1^0\tilde{\chi}_2^0$ cross-sections. They would be mostly higgsino for large M_2 and small μ, and in this case, the cross-section for $\tilde{\chi}_1^0\tilde{\chi}_2^0$ is such that the neutralino-specific searches can contribute significantly.

From the input parameters M_2, μ, $\tan\beta$, m_0 and A (the trilinear coupling), masses, production cross-sections and branching fractions are calculated according to the CMSSM [8, 9, 11, 12]. For each set of input parameters, the total number of $\tilde{\chi}_1^+\tilde{\chi}_1^-$ (for analyses (A)-(C)), $\tilde{\chi}_1^0\tilde{\chi}_2^0$ and $\tilde{\chi}_1^0\tilde{\chi}_3^0$ (for analyses (C)-(D)) $\tilde{\chi}_1^+\tilde{\chi}_1^-$, $\tilde{\chi}_1^\pm\tilde{\chi}_2^\mp$ and $\tilde{\chi}_2^+\tilde{\chi}_2^-$ (for analyses (E)-(F)) events expected to be observed is found using the known integrated luminosity, calculated cross-sections, branching ratios, and the detector efficiencies which depend upon the masses of these particles. The efficiency for detecting $\tilde{\chi}_1^0\tilde{\chi}_3^0$ events, even for decays through SUSY Higgs bosons, is found to be greater than for $\tilde{\chi}_1^0\tilde{\chi}_2^0$ events, so the efficiency functions for $\tilde{\chi}_1^0\tilde{\chi}_2^0$ were used to obtain conservative limits. The decay involving $\tilde{\chi}_{2,3}^0 \to \tilde{\ell}\ell$ when $m_{\tilde{\chi}_{2,3}^0} > m_{\tilde{\ell}}$ and the decay $\tilde{\chi}_{2,3}^0 \to \tilde{\chi}_1^0\gamma$ are assumed to be undetectable in this analysis.

Slepton and sneutrino masses, cross-sections, and branching ratios are also determined at each set of CMSSM parameters. When the minimum m_0 case is considered, the value of m_0 is decreased until it is just consistent with both $\tilde{\nu}$ mass limits [36] and the 95% C.L. upper limits on the product of cross-section and $\mathrm{BR}^2(\tilde{\ell} \to \ell\tilde{\chi}_1^0)$ for $\tilde{\mu}_R^+\tilde{\mu}_R^-$ and $\tilde{\mathrm{e}}_R^+\tilde{\mathrm{e}}_R^-$ pair production as given in Ref. [38].

The following regions of the CMSSM parameters are scanned: $0 \leq M_2 \leq 1500$ GeV, $|\mu| \leq 500$ GeV, and $A = \pm M_2$, $\pm m_0$ and 0. The typical scan step is 0.2 GeV. It has been checked that the scanned ranges of parameters are large enough that the exclusion regions change negligibly for larger ranges. No significant dependence on A is observed.

Using the results of analyses (A)-(D), the 95% C.L. upper limit on the expected number of events is determined as described previously. Figure 13 shows the resulting exclusion regions (shaded regions) in the (M_2,μ) plane for $\tan\beta = 1.5$ and 35. The region of M_2-μ excluded is enlarged significantly with respect to the results at $\sqrt{s} = 161$ GeV alone [3]. In the CMSSM the gauginos have a common mass, $m_{1/2}$, at the GUT scale, therefore the gluino mass ($M_3 \equiv m_{\tilde{g}}$) is directly related to M_2 by $M_3/M_2 = \alpha_s/\frac{\alpha}{\sin^2\theta_W}$. Figure 13 therefore includes a scale indicating the corresponding mass limits for gluinos.

The problem associated with $\tan\beta$ approaching 1.0 is clear from Fig. 14 where the region near $M_2 = \mu = 0$ is not excluded by results from analyses (A)-(D), or from the Z^0 width and direct neutralino searches at LEP1 [39]. For the case of $\tan\beta = 1.0$, the results from analyses (E) and (F) are therefore invoked, and the consequent excluded regions are shown as the hatched regions overlaid onto the regions excluded by analyses (A)-(D) in Fig. 14(a) and (b). The areas near $M_2 = \mu = 0$ not excluded by previous analyses are now excluded.

The restrictions on the CMSSM parameter space presented can be transformed into exclusion regions in ($m_{\tilde{\chi}_1^0}$,$m_{\tilde{\chi}_1^\pm}$) or ($m_{\tilde{\chi}_2^0}$,$m_{\tilde{\chi}_1^0}$) mass space. A given mass pair is considered excluded only if *all* CMSSM parameters in the scan which lead to the same values of mass pairs being considered are excluded at the 95% C.L. In the ($m_{\tilde{\chi}_1^0}$,$m_{\tilde{\chi}_1^\pm}$) plane, Fig. 15 shows the corresponding 95% C.L. exclusion regions for $\tan\beta = 1.0$, 1.5 and 35. The region extending beyond the kinematic limit for chargino pair production in Fig. 15(a) is due to the direct topological search for neutralinos at LEP1 [39] illustrated in Fig. 14. The analogous exclusion regions in the ($m_{\tilde{\chi}_1^0}$,$m_{\tilde{\chi}_2^0}$) plane are shown in Fig. 16. A smaller fraction of the accessible region of mass space for neutralino production is excluded because of the smaller predicted cross-sections for neutralinos. The portion of the excluded region extending beyond the kinematic limit

$(m_{\tilde{\chi}^0_1} + m_{\tilde{\chi}^0_2}) = 172$ GeV is due to the exclusion of chargino production for the relevant CMSSM parameters. The lower limits of the chargino and neutralino masses are listed in Table 18.

A similar procedure is followed for other values of $\tan\beta$ to find the lower limit on the mass of the $\tilde{\chi}^0_1$ as a function of $\tan\beta$ for $m_0 = 1$ TeV and minimum m_0 with the result shown in Fig. 17(a). Each lower limit on $m_{\tilde{\chi}^0_1}$ in Fig. 17(a) corresponds to a particular value of M_2, μ, $\tan\beta$, and minimum m_0 consistent with slepton mass limits. Figure 17(b) shows the corresponding sneutrino mass for those SUSY parameters where the lowest $\tilde{\chi}^0_1$ mass was found, as a function of $\tan\beta$.

Returning to the assumption of gauge unification at the GUT scale and the CMSSM, a limit on M_2 can be obtained as a function of m_0 for a given value of μ and $\tan\beta$. Under this assumption, limits on gluino and squark masses are then implied. The average of the $\tilde{u}_R$, $\tilde{u}_L$, $\tilde{d}_R$ and $\tilde{d}_L$ masses ($m_{\tilde{q}}$) can be calculated from m_0, M_2 and $\tan\beta$ (see equations (1)-(4)) in the CMSSM framework. Limits in the ($m_{\tilde{q}}$,$m_{\tilde{g}}$) plane can therefore be calculated and are shown in Fig. 18. The limit of Fig. 18(a) can be compared with the mass limit from current direct $\tilde{q}$ and $\tilde{g}$ searches at the Tevatron. For $\tan\beta = 4$ and $\mu = -400$ GeV, a gluino mass limit of 270 GeV was obtained for the case of $m_{\tilde{q}} > 500$ GeV. Under these assumptions the limit is significantly better than those obtained from direct searches by the CDF and D0 collaborations at the Tevatron [40, 41]. The CDF result is also shown in Fig. 18(a). In the region below the diagonal curve the lightest slepton or sneutrino mass becomes negative in the CMSSM framework.

6 Summary and Conclusion

A data sample corresponding to an integrated luminosity of 10.3 pb^{-1} at $\sqrt{s}$ =170 and 172 GeV collected with the OPAL detector has been analysed to search for pair production of charginos and neutralinos predicted by supersymmetric theories. The expected background for each search is 0.9 events and no candidate events are observed in either search. For the case of $\tan\beta$ close to 1.0, and $M_2 \approx \mu \approx 0$, a new search is performed and no evidence for an excess of W-pair-like events is observed. The exclusion limits on $\tilde{\chi}^\pm_1$ and $\tilde{\chi}^0_j$ production are significantly higher with respect to the results obtained by OPAL at $\sqrt{s}$ =130 GeV, 136 GeV [2] and 161 GeV [3]. The 95% C.L. lower mass limit of the chargino is close to the kinematic limit within the framework of the MSSM. Assuming that the lightest chargino is heavier than the

Mass	$\tan\beta = 1.0$		$\tan\beta = 1.5$		$\tan\beta = 35$	
GeV	Min. m_0	$m_0 = 1$ TeV	Min. m_0	$m_0 = 1$ TeV	Min. m_0	$m_0 = 1$ TeV
$m_{\tilde{\chi}^\pm_1}$	> 65.7	> 84.5	> 72.1	> 85.0	> 74.4	> 85.1
$m_{\tilde{\chi}^0_1}$	> 13.3	> 24.7	> 23.9	> 34.6	> 40.9	> 43.8
$m_{\tilde{\chi}^0_2}$	> 46.9	> 46.9	> 45.3	> 56.5	> 74.6	> 85.5
$m_{\tilde{\chi}^0_3}$	> 75.8	> 90.1	> 94.1	> 101.7	> 116.5	> 116.5

Table 18: Lower limits at 95% C.L. obtained on the lightest chargino mass, and the masses of the three lightest neutralinos, in GeV. These limits are given for $\Delta M_+ \geq 10$ GeV and $\Delta M_0 \geq 10$ GeV. Two cases are considered: $m_0 = 1$ TeV and the smallest m_0 possible that complies with the LEP1 $\tilde{\nu}$ and OPAL $\tilde{\ell}$ limits.

lightest neutralino by more than 10 GeV, a lightest chargino mass limit at 95% C.L. of 84.5 GeV is obtained (for $\tan\beta \geq 1.0$) if the universal scalar mass, m_0, is larger than 1 TeV. The mass limit is 65.7 GeV for the smallest m_0 compatible with limits on sneutrino masses and OPAL limits on slepton masses. The lower limit on the lightest neutralino mass ($m_{\tilde{\chi}_1^0}$) at 95% C.L. for $\tan\beta \geq 1.0$ is 24.7 GeV for $m_0 = 1$ TeV and 13.3 GeV for the minimum m_0 scenario. These limits are also given as functions of $\tan\beta$ and are generally higher for larger values of $\tan\beta$. If limits on M_2 are interpreted in the framework of the CMSSM, limits on gluino and squark masses are complementary to those obtained from direct searches.

Acknowledgements

We particularly wish to thank the SL Division for the efficient operation of the LEP accelerator at all energies and for their continuing close cooperation with our experimental group. We thank our colleagues from CEA, DAPNIA/SPP, CE-Saclay for their efforts over the years on the time-of-flight and trigger systems which we continue to use. In addition to the support staff at our own institutions we are pleased to acknowledge the
Research Corporation, USA,
Department of Energy, USA,
National Science Foundation, USA,
Particle Physics and Astronomy Research Council, UK,
Natural Sciences and Engineering Research Council, Canada,
Israel Science Foundation, administered by the Israel Academy of Science and Humanities,
Minerva Gesellschaft,
Benoziyo Center for High Energy Physics,
Japanese Ministry of Education, Science and Culture (the Monbusho) and a grant under the Monbusho International Science Research Program,
German Israeli Bi-national Science Foundation (GIF),
Bundesministerium für Bildung, Wissenschaft, Forschung und Technologie, Germany,
National Research Council of Canada,
Hungarian Foundation for Scientific Research, OTKA T-016660, T023793 and OTKA F-023259.

References

[1] Y. Gol'fand and E. Likhtam, JETP Lett. **13** (1971) 323;
D. Volkov and V. Akulov, Phys. Lett. **B46** (1973) 109;
J. Wess and B. Zumino, Nucl. Phys. **B70** (1974) 39.

[2] OPAL Collab., G. Alexander *et al.*, Phys. Lett. **B377** (1996) 181.

[3] OPAL Collab., K. Ackerstaff *et al.*, CERN preprint CERN-PPE/96-135 (1996).

[4] ALEPH Collab., D. Buskulic *et al.*, Phys. Lett. **B373** (1996) 246;
DELPHI Collab., P. Abreu *et al.*, 'Search for the lightest chargino at $\sqrt{s}$ = 130 and

136 GeV in DELPHI', CERN preprint CERN-PPE/96-75 (1996);
L3 Collab., M. Acciarri *et al.*, Phys. Lett. **B377** (1996) 289.

[5] CDF Collab., F. Abe *et al.*, Phys. Rev. Lett. **76** (1996) 4307;
D0 Collab., S. Abachi *et al.*, Phys. Rev. Lett. **76** (1996) 2228.

[6] P. Fayet, *Unification of the Fundamental Particle Interactions*, Plenum Press (1980) 587.

[7] H. P. Nilles, Phys. Rep. **110** (1984) 1;
H. E. Haber and G. L. Kane, Phys. Rep. **117** (1985) 75.

[8] A. Bartl, H. Fraas and W. Majerotto, Z. Phys. **C30** (1986) 441;
A. Bartl, H. Fraas and W. Majerotto, Z. Phys. **C41** (1988) 475;
A. Bartl, H. Fraas, W. Majerotto and B. Mösslacher, Z. Phys. **C55** (1992) 257.

[9] M. Chen, C. Dionisi, M. Martinez and X. Tata, Phys. Rep. **159** (1988) 201;
J. L. Feng and M. J. Strassler, Phys. Rev. **D51** (1995) 4661.

[10] H. Haber and D. Wyler, Nucl. Phys. **B323** (1989) 267.

[11] A. Bartl, H. Fraas and W. Majerotto, Nucl. Phys. **B278** (1986) 1;
S. Ambrosanio and B. Mele, Phys. Rev. **D52** (1995) 3900.

[12] M. Carena, J.R. Espinosa, M. Quiros and C.E.M. Wagner, Phys. Lett. **355B** (1995) 209.

[13] K. Inoue, A. Kakuto, H. Komatsu and S. Takeshita, Prog. Theor. Phys. **68** (1982) 927, *ibid* **71** (1984) 413;
M. Drees and M. M. Nojiri, Nucl. Phys. **B369** (1992) 54

[14] M. Carena, S. Dimopoulos, S. Raby and C.M.E. Wagner, Phys. Rev. **D52** (1995) 4133.

[15] B. Ananthanarayan, K.S. Babu and Q. Shafi, Nucl. Phys. **B428** (1994) 19, and references therein.

[16] ALEPH Collab., B. Buskulic *et al.* Z. Physik **C72** (1996) 549.

[17] E. Accomando *et al.*, 'Event Generators for Discovery Physics', hep-ph/9602203, Feb. 1996, and in 'Physics at LEP2', eds. G. Altarelli, T. Sjöstrand and F. Zwirner, CERN 96-01, vol.2 (1996) 299.

[18] OPAL Collab., K. Ahmet *et al.*, Nucl. Instr. Meth. **A305** (1991) 275;
P.P. Allport *et al.*, Nucl. Instr. Meth. **A346** (1994) 476;
B.E. Anderson *et al.*, IEEE Trans. on Nucl. Science **41** (1994) 845.

[19] C. Dionisi *et al.*, in 'Physics at LEP2', eds. G. Altarelli, T. Sjöstrand and F. Zwirner, CERN 96-01, vol.2 (1996) 337.

[20] T. Sjöstrand, Comp. Phys. Comm. **39** (1986) 347;
T. Sjöstrand, PYTHIA 5.7 and JETSET 7.4 Manual, CERN-TH 7112/93.

[21] E. Boudinov *et al.*, '$\gamma\gamma$ Event Generators', hep-ph/9512371, Dec. 1995, and in 'Physics at LEP2', eds. G. Altarelli, T. Sjöstrand and F. Zwirner, CERN 96-01, vol.2 (1996) 187.

[22] G. Marchesini *et al.*, Comp. Phys. Comm. **67** (1992) 465.

[23] J. Fujimoto *et al.*, KEK-CP-046 (1996).

[24] J.A.M. Vermaseren, Nucl. Phys. **B229** (1983) 347.

[25] F.A. Berends, R. Pittau, R. Kleiss, Comp. Phys. Comm. **85** (1995) 437.

[26] S. Jadach, B. F. L. Ward, Z. Wąs, Comp. Phys. Comm. **79** (1994) 503.

[27] S. Jadach, W. Płaczek, B.F.L. Ward, in 'Physics at LEP2', eds. G. Altarelli, T. Sjöstrand and F. Zwirner, CERN 96-01, vol. 2 (1996).

[28] J. Allison *et al.*, Nucl. Instr. Meth. **A317** (1992) 47.

[29] N. Brown and W.J. Stirling, Phys. Lett. **B252** (1990) 657;
S. Bethke, Z. Kunszt, D. Soper and W.J. Stirling, Nucl. Phys. **B370** (1992) 310;
S. Catani, Phys. Lett. **B269** (1991) 432;
N. Brown and W.J. Stirling, Z. Phys. **C53** (1992) 629.

[30] OPAL Collab., R. Akers *et al.*, Phys. Lett. **B327** (1994) 411.

[31] OPAL Collab., R. Akers *et al.*, Z. Phys. **C65** (1994) 17.

[32] OPAL Collab., P. Acton *et al.*, Z. Phys. **C58** (1993) 523.

[33] OPAL Collab., R. Akers *et al.*, Z. Phys. **C60** (1993) 199.

[34] OPAL Collab., G. Alexander *et al.*, Z. Phys. **C52** (1991) 175.

[35] OPAL Collab., K. Ackerstaff *et al.*, Phys. Lett. **B393** (1997) 231.

[36] Particle Data Group, Phys. Rev. **D50** (1994) 1173.

[37] R.D. Cousins and V.L. Highland, Nucl. Instr. Meth. **A320** (1992) 331.

[38] OPAL Collab., K. Ackerstaff *et al.*, Phys. Lett. **B396** (1997) 301.

[39] OPAL Collab., G. Alexander *et al.*, Phys. Lett. **B377** (1996) 273.

[40] CDF Collaboration, F. Abe *et al.*, FERMILAB-PUB-97/031-E (1997),
submitted to Phys. Rev. D, Rapid Communications.

[41] D0 Collab., S. Abachi *et al.*, Phys. Rev. Lett. **75** (1995) 618.

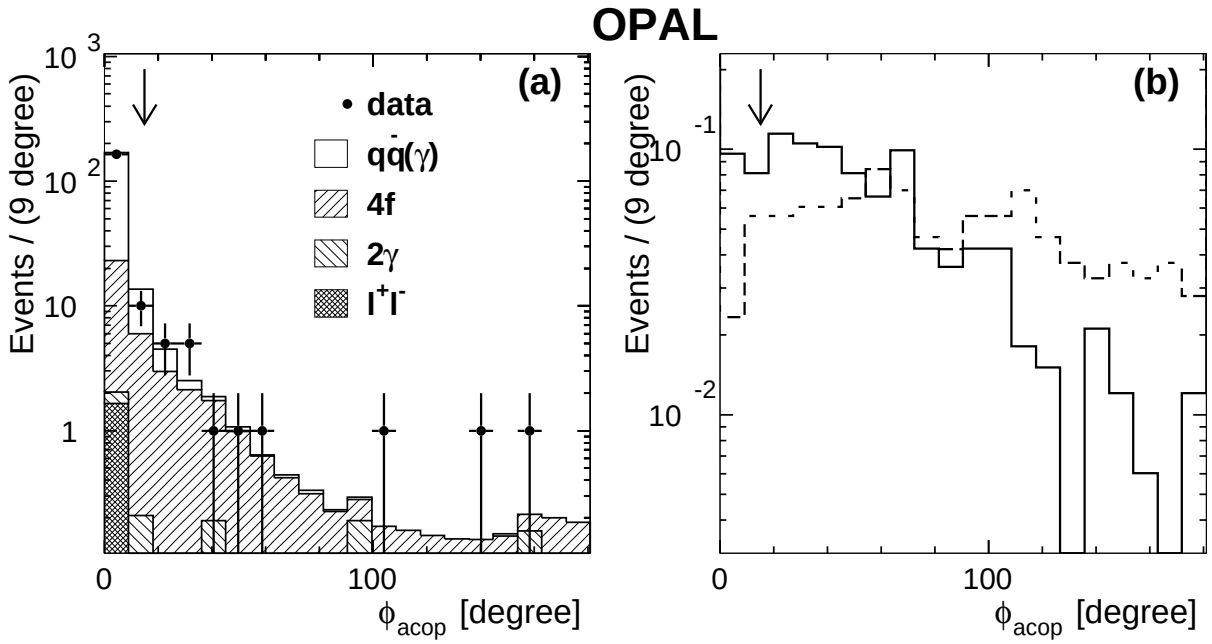

Figure 1: The distributions of the acoplanarity angle, $\phi_{\rm acop}$, after cut (A2). In (a) are shown the predicted contributions from background processes: dilepton events (double hatched area), two-photon processes (negative slope hatching area), four-fermion processes (including W-pair events) (positive slope hatched area), and multihadronic events (open area). In each case the distribution has been normalized to 10.3 pb^{-1}. Also shown in (a) is the distribution of the data (dark circles). In (b) predictions from simulated chargino events are shown for $m_{\tilde{\chi}_1^\pm} = 80$ GeV and $m_{\tilde{\chi}_1^0} = 60$ GeV (solid line histogram) and for $m_{\tilde{\chi}_1^\pm} = 80$ GeV and $m_{\tilde{\chi}_1^0} = 20$ GeV (dotted line histogram). The arrows shown indicate the position of the cut used in the event selection.

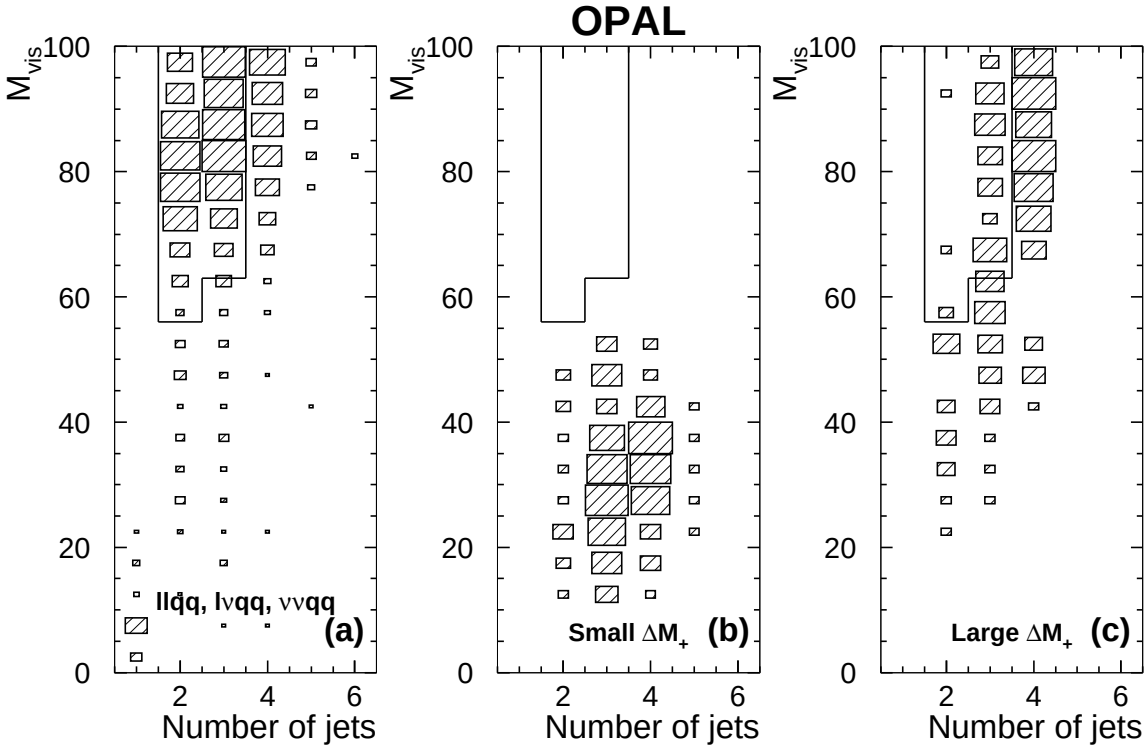

Figure 2: The distributions of the $M_{\rm vis}$ versus $\rm N_{jets}$ after cut (A4). Distributions of chargino signal events are shown in (b) for $m_{\tilde{\chi}_1^\pm} = 80$ GeV and $m_{\tilde{\chi}_1^0} = 60$ GeV and in (c) for $m_{\tilde{\chi}_1^\pm} = 80$ GeV and $m_{\tilde{\chi}_1^0} = 20$ GeV. The background from $\ell\ell\mathrm{q}\bar{\mathrm{q}}$, $\nu\ell\mathrm{q}\bar{\mathrm{q}}'$ and $\nu\nu\mathrm{q}\bar{\mathrm{q}}$ is shown in (a). Events with two or three jets are rejected in the region outlined by the thin line in the plots.

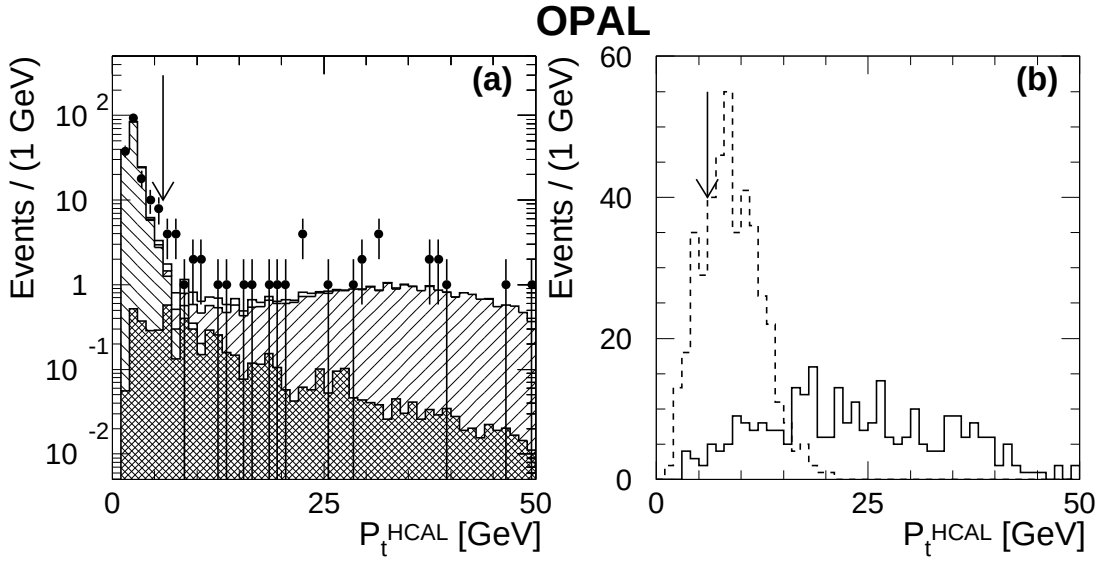

Figure 3: The distribution of $P_t^{\rm HCAL}$ in analysis (B) after cut (B1). Data and expected background contributions are shown in (a). The background sources are labelled as in Fig. 1. The distribution of the signal for simulated chargino events with $m_{\tilde{\chi}_1^+} = 80$ GeV and $m_{\tilde{\chi}_1^0} = 40$ GeV (solid histogram) and with $m_{\tilde{\chi}_1^+} = 80$ GeV and $m_{\tilde{\chi}_1^0} = 70$ GeV (dashed histogram) are shown in (b). The normalizations of the signal distributions are arbitrary.

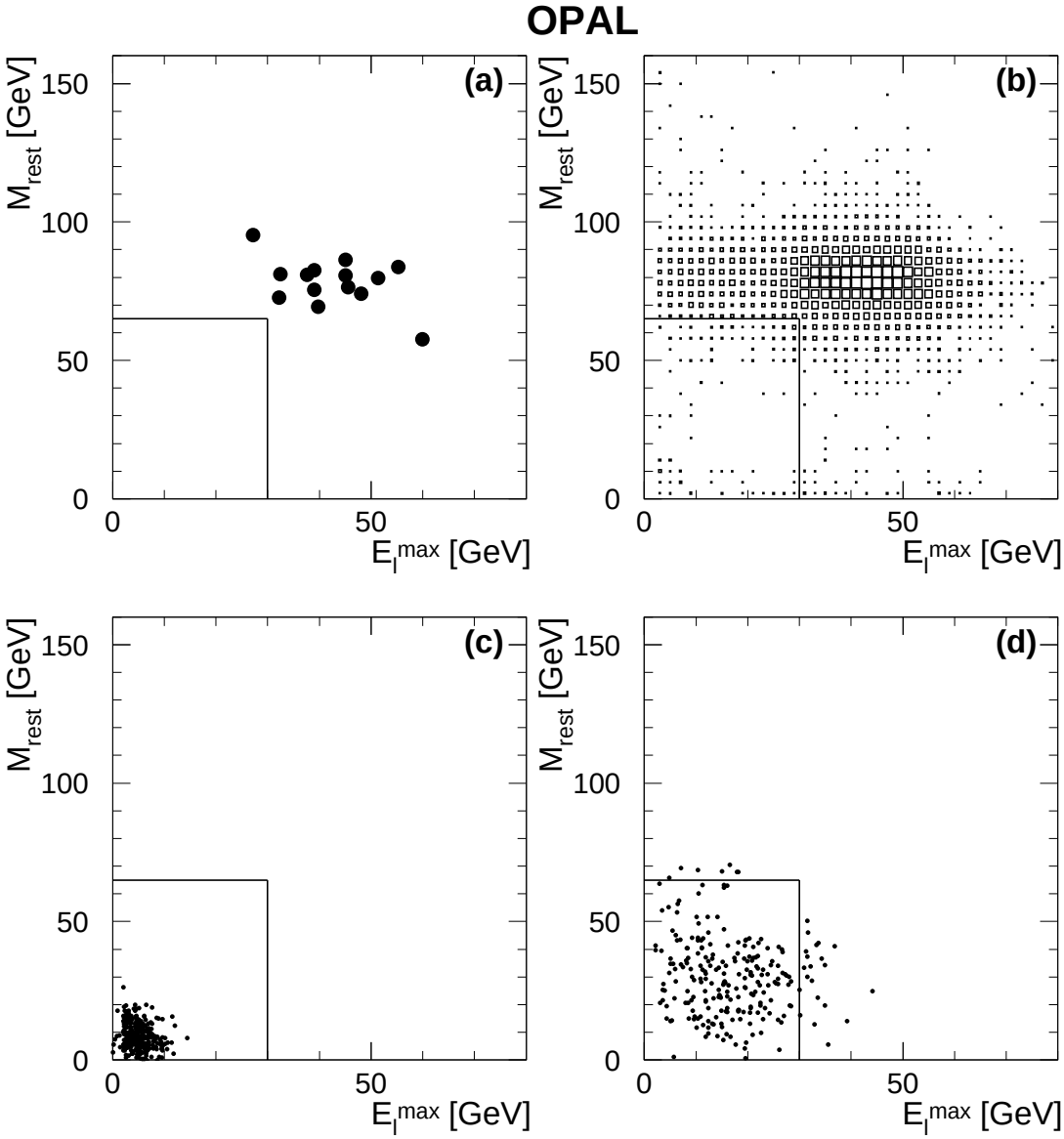

Figure 4: Scatter plots of $M_{\rm rest}$ vs. $E_\ell^{\rm max}$ after cut (B3). Figure (a) shows the data. The Monte Carlo prediction for four-fermion background is shown in (b). The other figures show the distribution of the signal for simulated chargino events with $m_{\tilde{\chi}_1^+} = 80$ GeV and $m_{\tilde{\chi}_1^0} = 70$ GeV (c) and with $m_{\tilde{\chi}_1^+} = 80$ GeV and $m_{\tilde{\chi}_1^0} = 40$ GeV (d). The straight lines in all figures indicate the selection criteria.

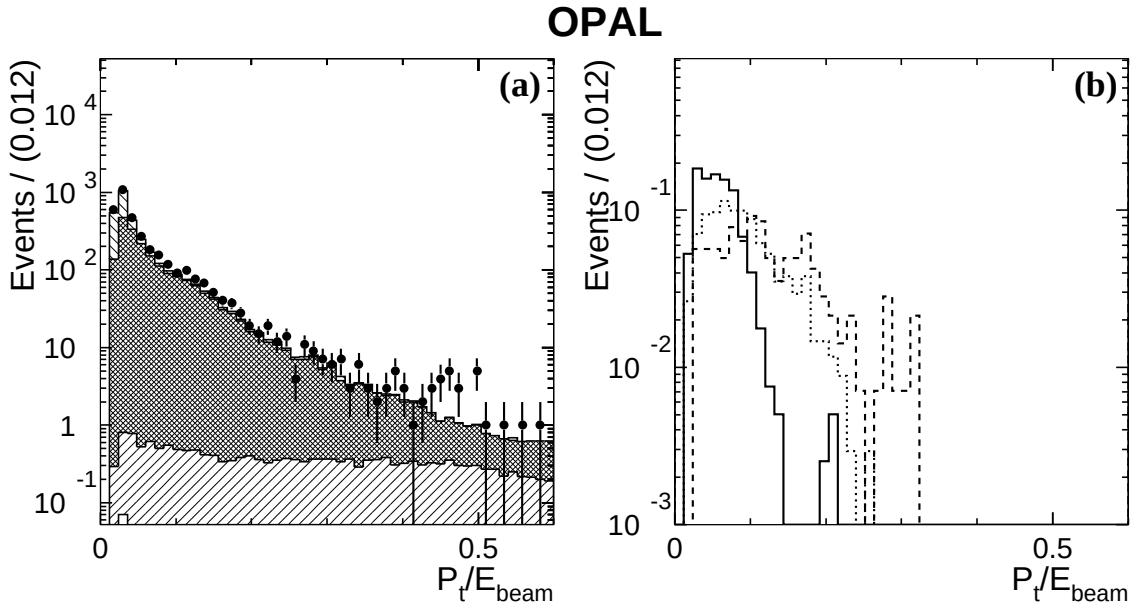

Figure 5: The distributions of $P_t/E_{\rm beam}$ for all $\phi_{\rm acop}$ after preselection, for events in analysis (C). Data and background contributions are shown in (a). The background sources are labelled as in Fig. 1. In (b) predictions from the simulation for chargino and neutralino events are shown: $m_{\tilde{\chi}_1^+} = 70$ GeV, $\Delta M_+ = 5$ GeV (solid line), $m_{\tilde{\chi}_1^+} = 80$ GeV, $\Delta M_+ = 20$ GeV (dashed line), $m_{\tilde{\chi}_2^0} + m_{\tilde{\chi}_1^0} = 130$ GeV, $\Delta M_0 = 10$ GeV (dotted line). The normalizations of the signal distributions are arbitrary.

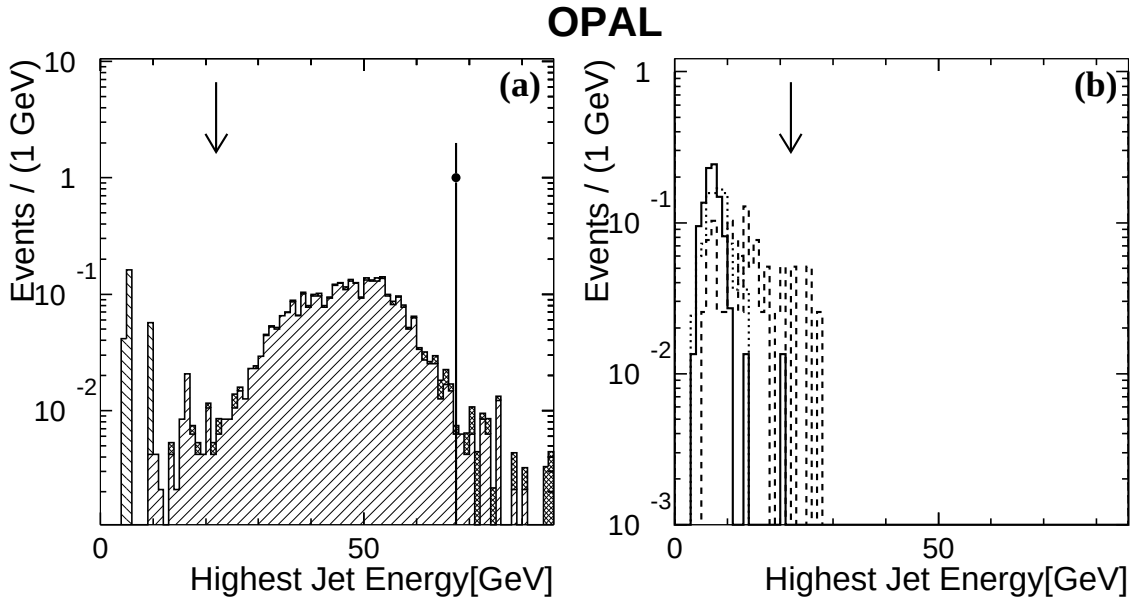

Figure 6: The distributions of the jet energy of the events in category (C) after all the other cuts were applied. Data and background contributions are shown in (a). The background sources are labelled as in Fig. 1. The Monte Carlo signal distributions are shown in (b) and are labelled as in Fig. 5. The normalizations of the signal distributions are arbitrary.

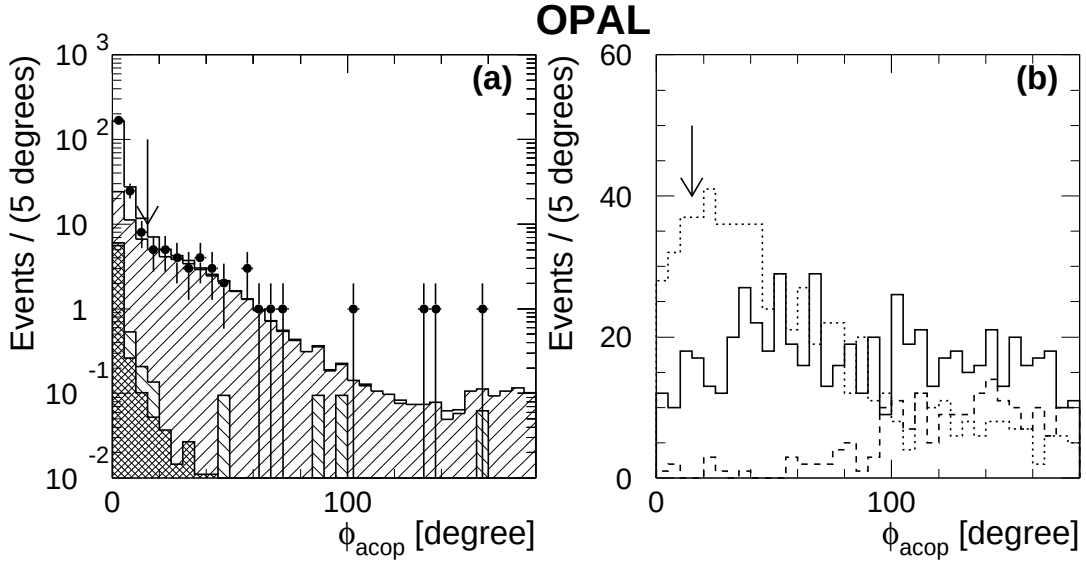

Figure 7: The distribution of the acoplanarity angle in analysis (D) after cut (D2). Data and background prediction from the simulation are shown in (a). The background sources are labelled as in Fig. 1. In (b) Monte Carlo predictions from $\tilde{\chi}_1^0\tilde{\chi}_2^0$ events are given for $m_{\tilde{\chi}_2^0} = 95$ GeV and $m_{\tilde{\chi}_1^0} = 65$ GeV (solid line), $m_{\tilde{\chi}_2^0} = 85$ GeV and $m_{\tilde{\chi}_1^0} = 75$ GeV (dashed line) and $m_{\tilde{\chi}_2^0} = 115$ GeV and $m_{\tilde{\chi}_1^0} = 45$ GeV (dotted line). The normalizations of the signal distributions are arbitrary.

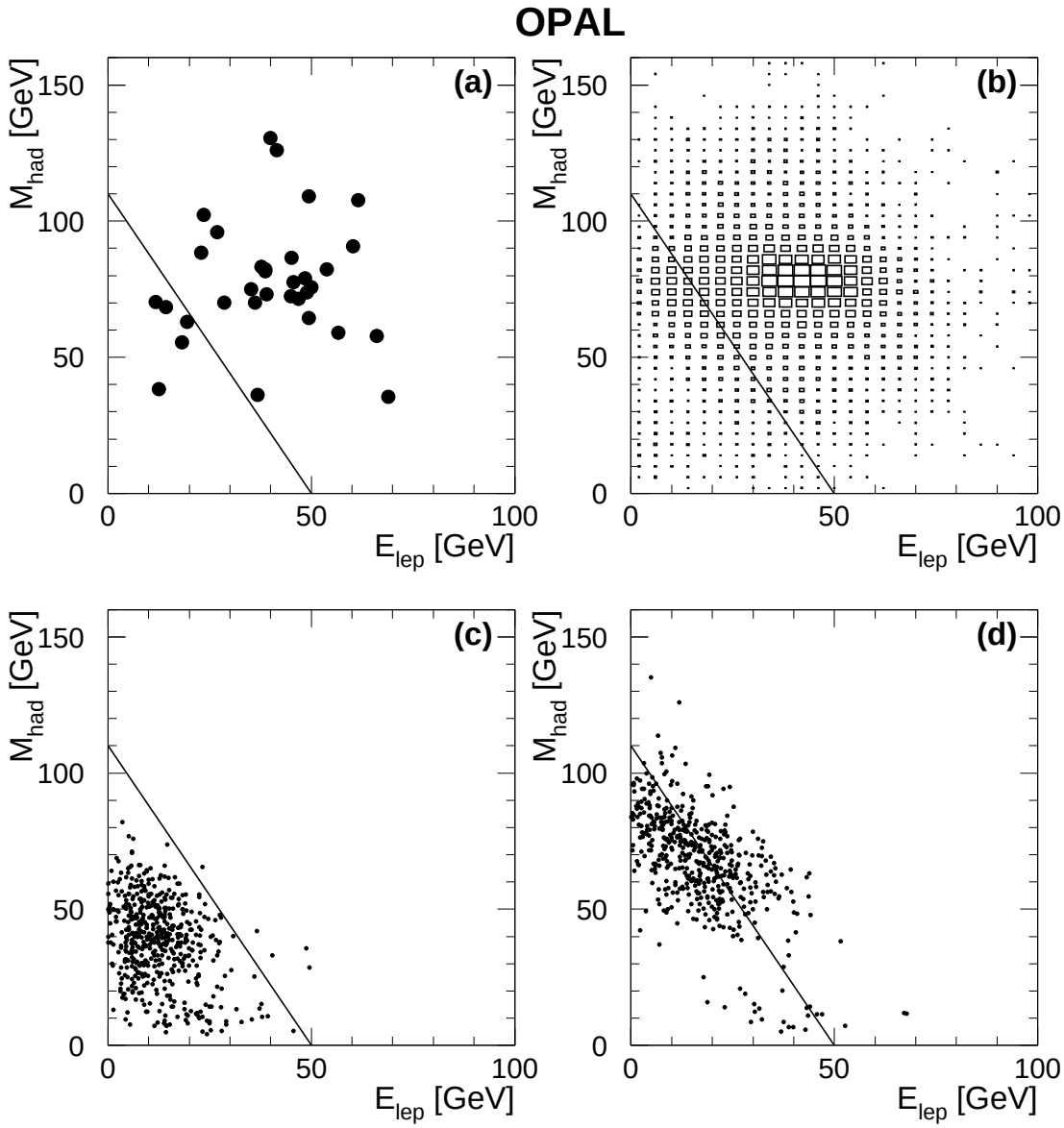

Figure 8: Scatter plots of M_{had} versus E_{lep} in analysis (D) after cut (D3) for those events whose M_{vis} is larger than 20 GeV. The data are shown in (a). Figure (b) shows the Monte Carlo prediction for the four-fermion background. In figures (c) and (d) signal distributions from simulated $\tilde{\chi}_1^0\tilde{\chi}_2^0$ events are given for $m_{\tilde{\chi}_2^0} = 115$ GeV and $m_{\tilde{\chi}_1^0} = 45$ GeV (c) and $m_{\tilde{\chi}_2^0} = 135$ GeV and $m_{\tilde{\chi}_1^0} = 25$ GeV (d). The straight lines in these figures indicate the selection cut.

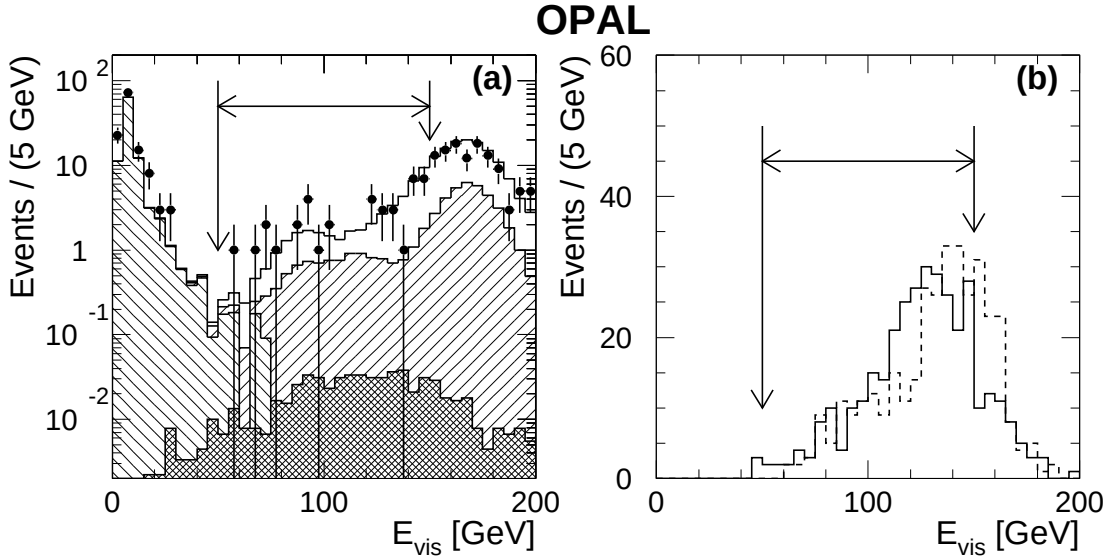

Figure 9: The distribution of $E_{\rm vis}$ in analysis (E) after cut (E3). Data and expected Monte Carlo background contributions are shown in (a). The background sources are labelled as in Fig. 1. The distributions of the signal for simulated chargino events with $m_{\tilde{\chi}_1^+} = 80$ GeV and $m_{\tilde{\chi}_1^0} = 0.6$ GeV with the $\tilde{\chi}_1^+ \to \tilde{\chi}_1^0 \mathrm{W}^{(*)}$ decay (solid histogram) and $m_{\tilde{\chi}_1^+} = 80$ GeV, $m_{\tilde{\chi}_2^0} = 2$ GeV and $m_{\tilde{\chi}_1^0} = 0.6$ GeV with the cascade decay $\tilde{\chi}_1^+ \to \tilde{\chi}_2^0 \mathrm{W}^{(*)} \to \tilde{\chi}_1^0 \gamma \mathrm{W}^{(*)}$ (dashed histogram) are shown in (b). The normalizations of the signal distributions are arbitrary.

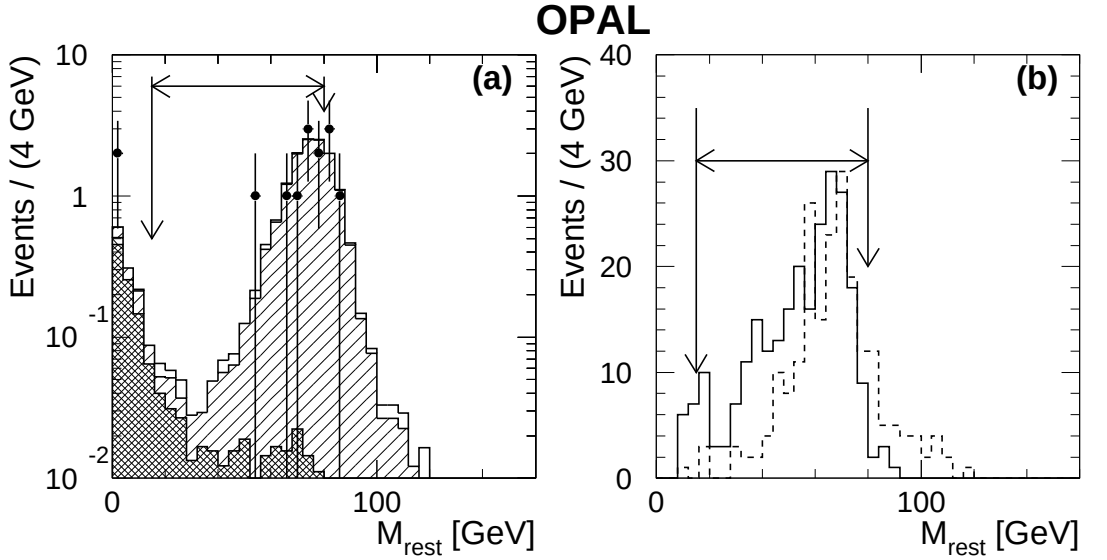

Figure 10: The distribution of $M_{\rm rest}$ in analysis (F) after cut (F4). Data and expected Monte Carlo background contributions are shown in (a). The background sources are labelled as in Fig. 1. The distributions of the signal for simulated chargino events with $m_{\tilde{\chi}_1^+} = 80$ GeV and $m_{\tilde{\chi}_1^0} = 0.6$ GeV with the $\tilde{\chi}_1^+ \to \tilde{\chi}_1^0 \mathrm{W}^{(*)}$ decay (solid histogram) and $m_{\tilde{\chi}_1^+} = 80$ GeV, $m_{\tilde{\chi}_2^0} = 2$ GeV and $m_{\tilde{\chi}_1^0} = 0.6$ GeV with the cascade decay $\tilde{\chi}_1^+ \to \tilde{\chi}_2^0 \mathrm{W}^{(*)} \to \tilde{\chi}_1^0 \gamma \mathrm{W}^{(*)}$ (dashed histogram) are shown in (b). The normalizations of the signal distributions are arbitrary.

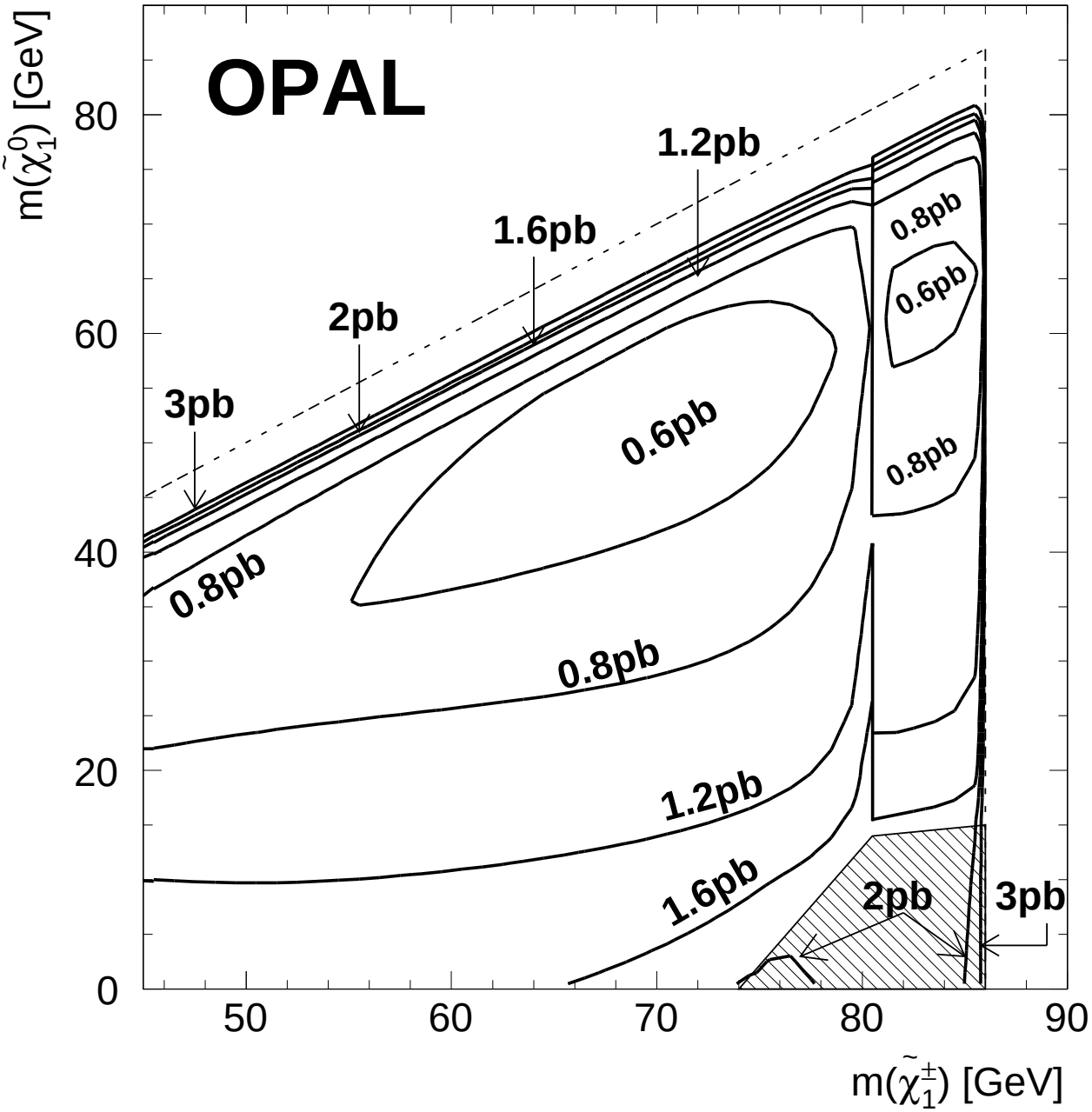

Figure 11: The contours of the 95% C.L. upper limits for the $e^+e^- \to \tilde{\chi}_1^+\tilde{\chi}_1^-$ production cross-sections at $\sqrt{s} = 172$ GeV are shown assuming $\mathrm{Br}(\tilde{\chi}_1^+ \to \tilde{\chi}_1^0 W^{*+}) = 100\%$. These limits have been obtained by combining the results from 161, 170 and 172 GeV assuming that the cross-sections scale with $\tilde{\beta}/s$, as described in the text. The hatched area indicates the region where analyses (E) and (F) contribute.

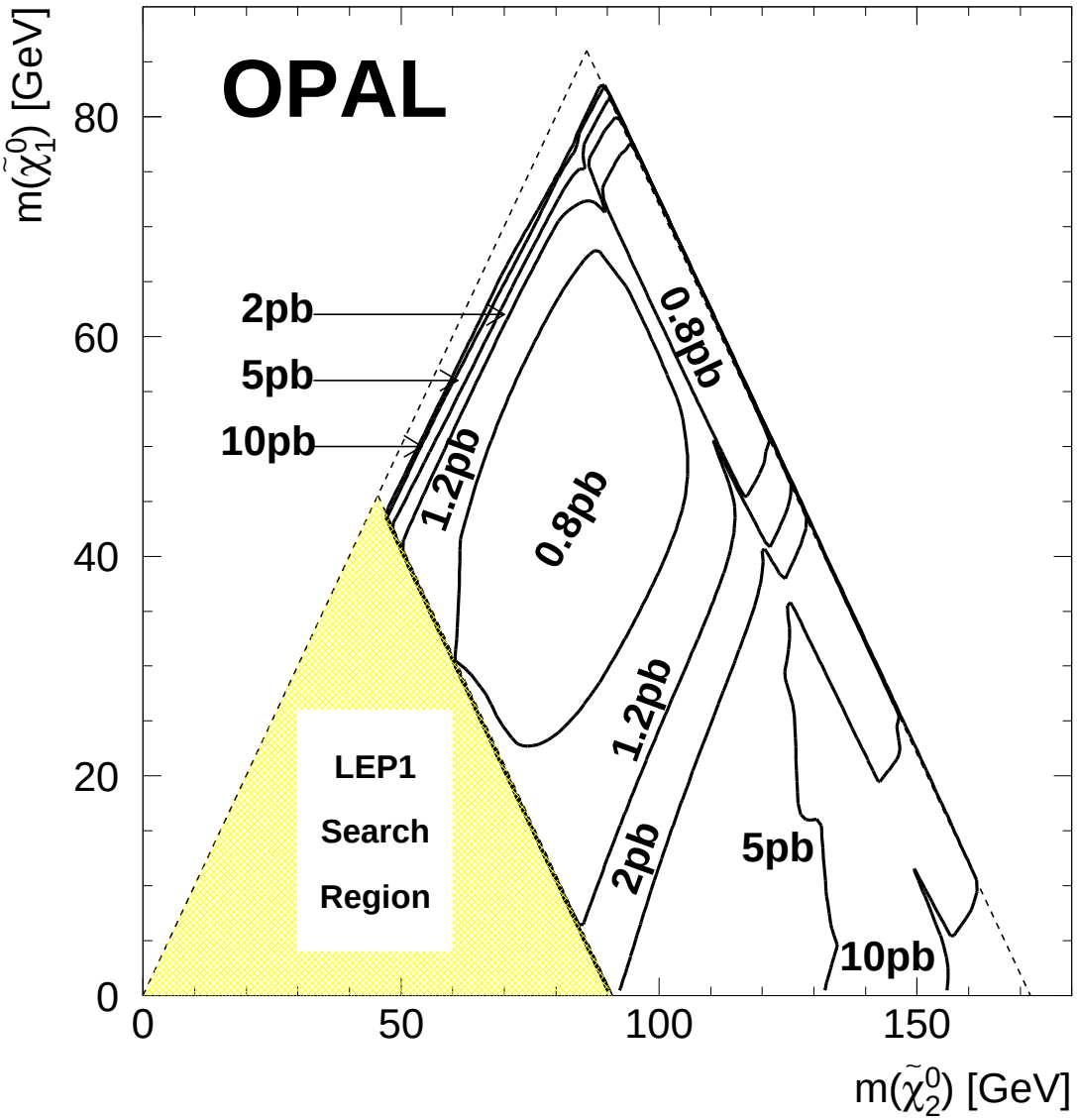

Figure 12: The contours of the 95% C.L. upper limits for the $e^+e^- \to \tilde{\chi}_2^0\tilde{\chi}_1^0$ production cross-sections at $\sqrt{s}$ =172 GeV are shown assuming $\mathrm{Br}(\tilde{\chi}_2^0 \to \tilde{\chi}_1^0 Z^*) = 100\%$. The region for which $(m_{\tilde{\chi}_2^0} + m_{\tilde{\chi}_1^0}) < m_Z$ is not considered in this analysis. These limits have been obtained by combining the results from 161, 170 and 172 GeV assuming that the cross-sections scale with $\sqrt{\tilde{\beta}_1 \cdot \tilde{\beta}_2}/s$, as described in the text.

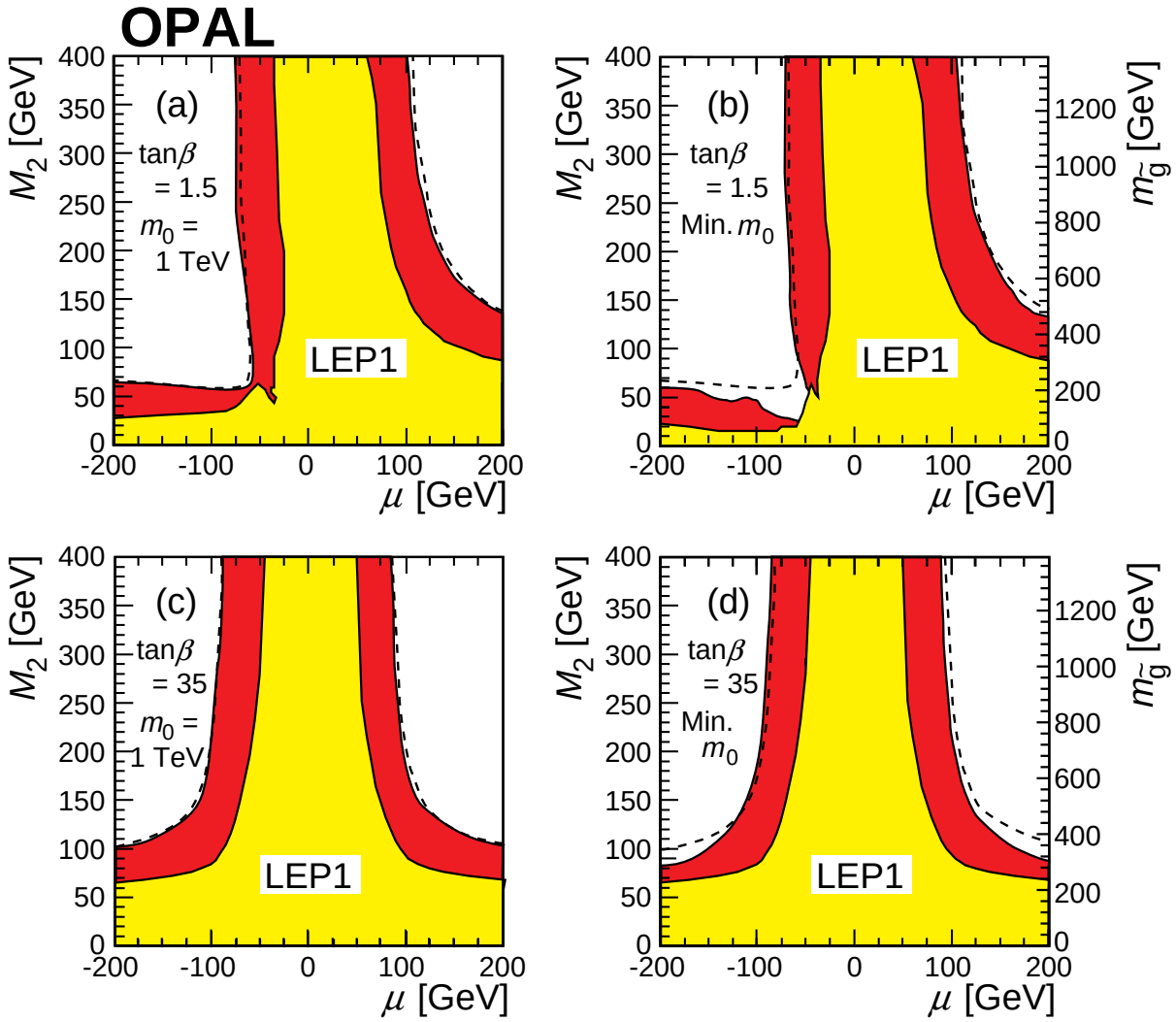

Figure 13: Exclusion regions at 95% C.L. in the (M_2,μ) plane for (a) $\tan\beta = 1.5$ and $m_0 = 1$ TeV, (b) $\tan\beta = 1.5$ and the minimum m_0 case (see text for details), (c) $\tan\beta = 35$ and $m_0 = 1$ TeV, and (d) $\tan\beta = 35$ and the minimum m_0 case. The light shaded areas show the LEP1 excluded regions and the dark shaded areas show the additional excluded region using the data from $\sqrt{s} = 161$ GeV combined with those from 170 and 172 GeV. The kinematical boundary for $\tilde{\chi}_1^+\tilde{\chi}_1^-$ production is shown by the dashed curves. The corresponding mass limits on the gluino mass, $m_{\tilde{g}}$, in the CMSSM are also shown.

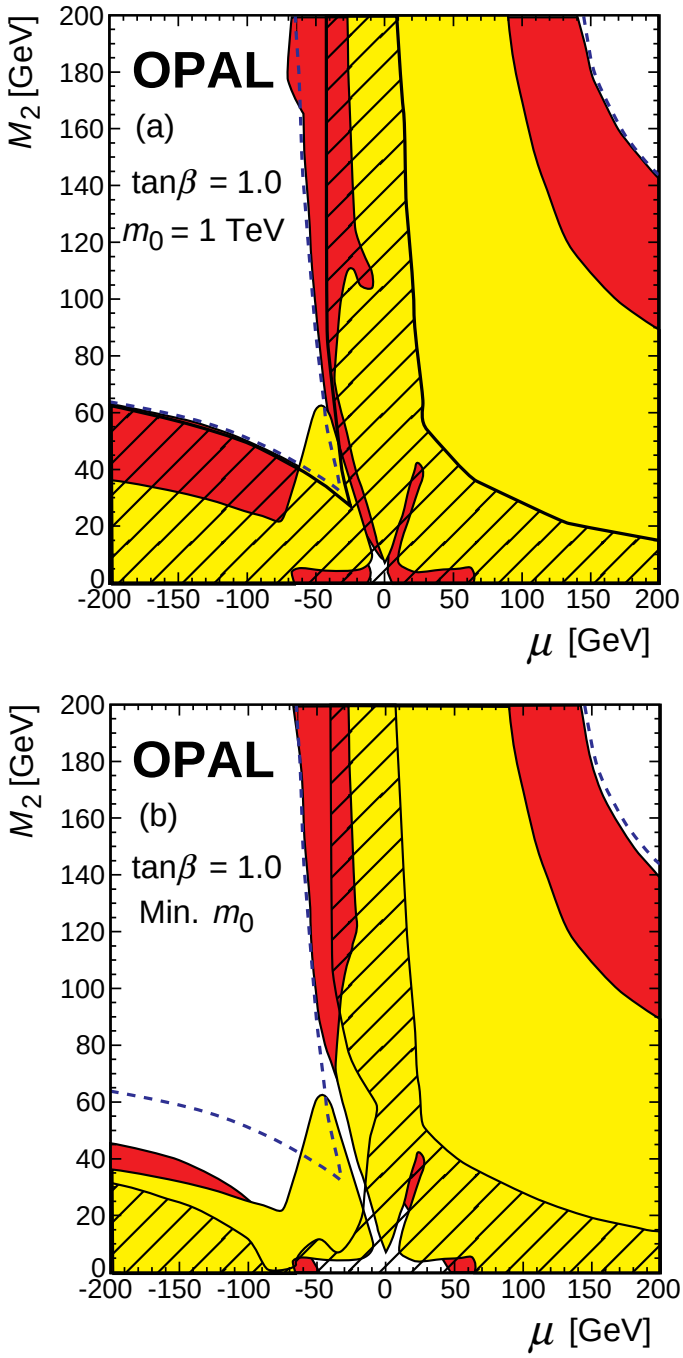

Figure 14: Exclusion regions at 95% C.L. in the (M_2,μ) plane for (a) $\tan\beta = 1.0$ and $m_0 = 1$ TeV, and (b) for the the minimum m_0 case. The light shaded areas show the LEP1 excluded regions [39], and the dark shaded areas show the additional excluded region using analyses (A)-(D) and the data from $\sqrt{s} = 161 - 172$ GeV. The hatched area shows the excluded region obtained with analyses (E) and (F) and the data at $\sqrt{s} = 170 - 172$ GeV. The kinematical boundary for $\tilde{\chi}_1^+\tilde{\chi}_1^-$ production is shown by the dashed curves.

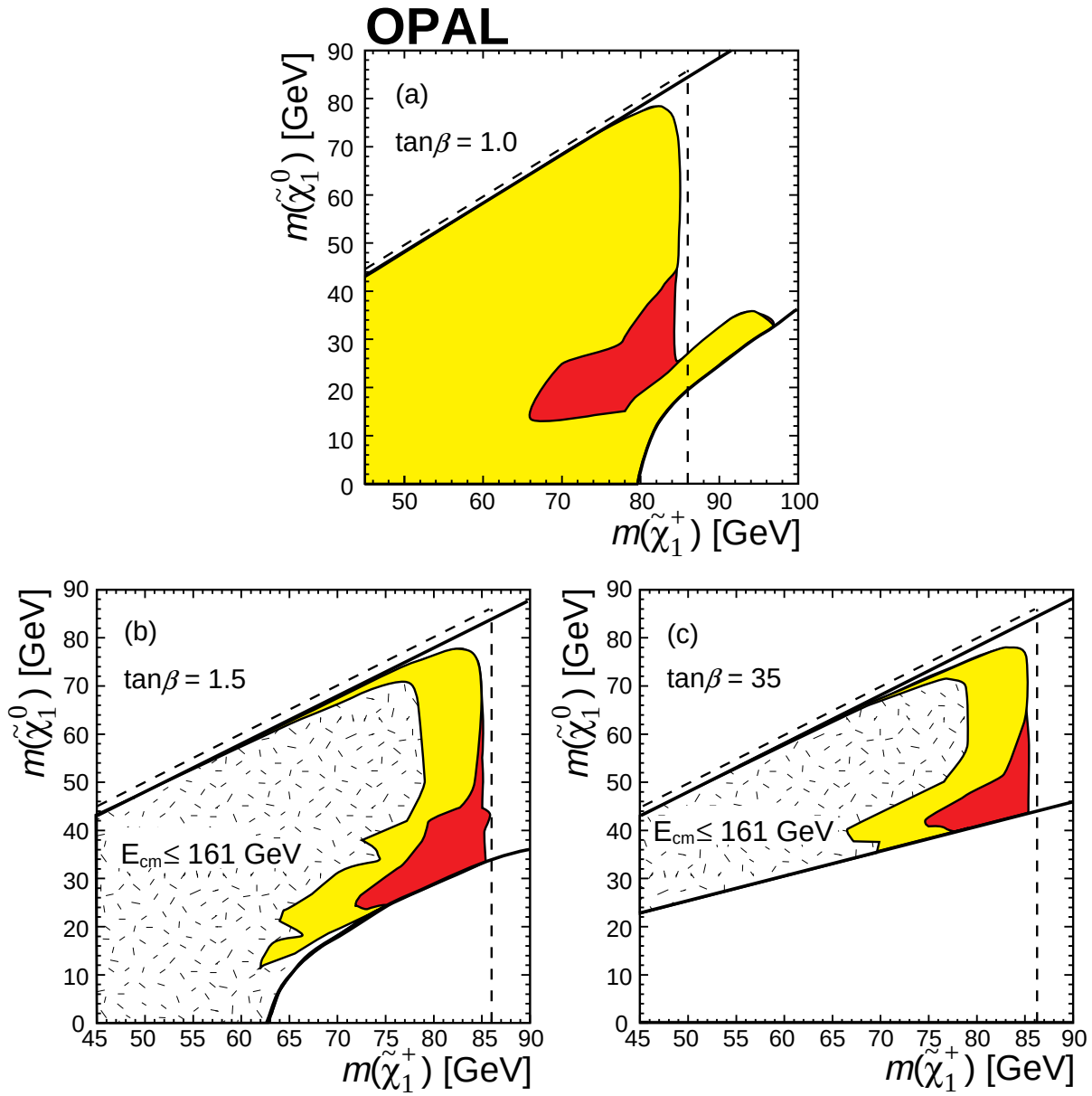

Figure 15: The 95% C.L. excluded region in the ($m_{\tilde{\chi}_1^+}$,$m_{\tilde{\chi}_1^0}$) plane within the framework of the MSSM for the case of minimum m_0 (light shaded region) and $m_0 = 1$ TeV (including also dark shaded region) for (a) $\tan\beta = 1.0$, (b) $\tan\beta = 1.5$ and (c) $\tan\beta = 35$. The region excluded by the analysis of LEP1, LEP1.5 [2] and 161 GeV [3] data is also shown in (b) and (c) for the minimum m_0 case (speckled region). The thick solid lines represent the theoretical bounds of the MSSM parameter space as given in the text. The kinematical boundaries for $\tilde{\chi}_1^+\tilde{\chi}_1^-$ production and decay at $\sqrt{s} = 172$ GeV are shown by dashed lines.

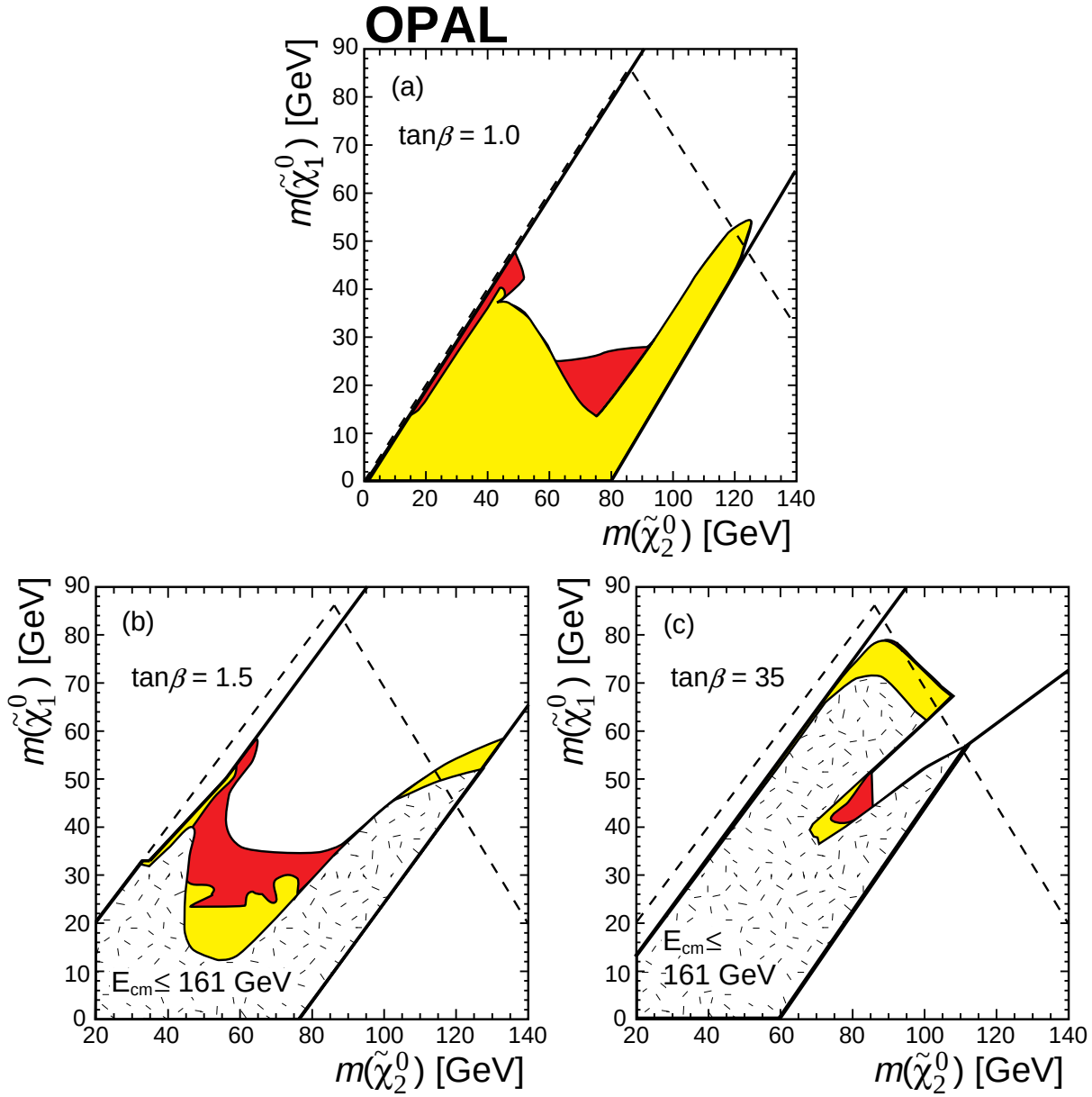

Figure 16: The 95% C.L. excluded region in the $(m_{\tilde{\chi}_2^0}, m_{\tilde{\chi}_1^0})$ plane within the framework of the MSSM for the case of minimum m_0 (light shaded region) and $m_0 = 1$ TeV (including also dark shaded region) for (a) $\tan\beta = 1.0$, (b) $\tan\beta = 1.5$ and (c) $\tan\beta = 35$. The region excluded by the analysis of LEP1, LEP1.5 [2] and 161 GeV [3] data is also shown in (b) and (c) for the minimum m_0 case (speckled region). The thick solid lines represent the theoretical bounds of the MSSM parameter space as given in the text. The kinematical boundaries for $\tilde{\chi}_1^0\tilde{\chi}_2^0$ production and decay at $\sqrt{s} = 172$ GeV are shown by dashed lines.

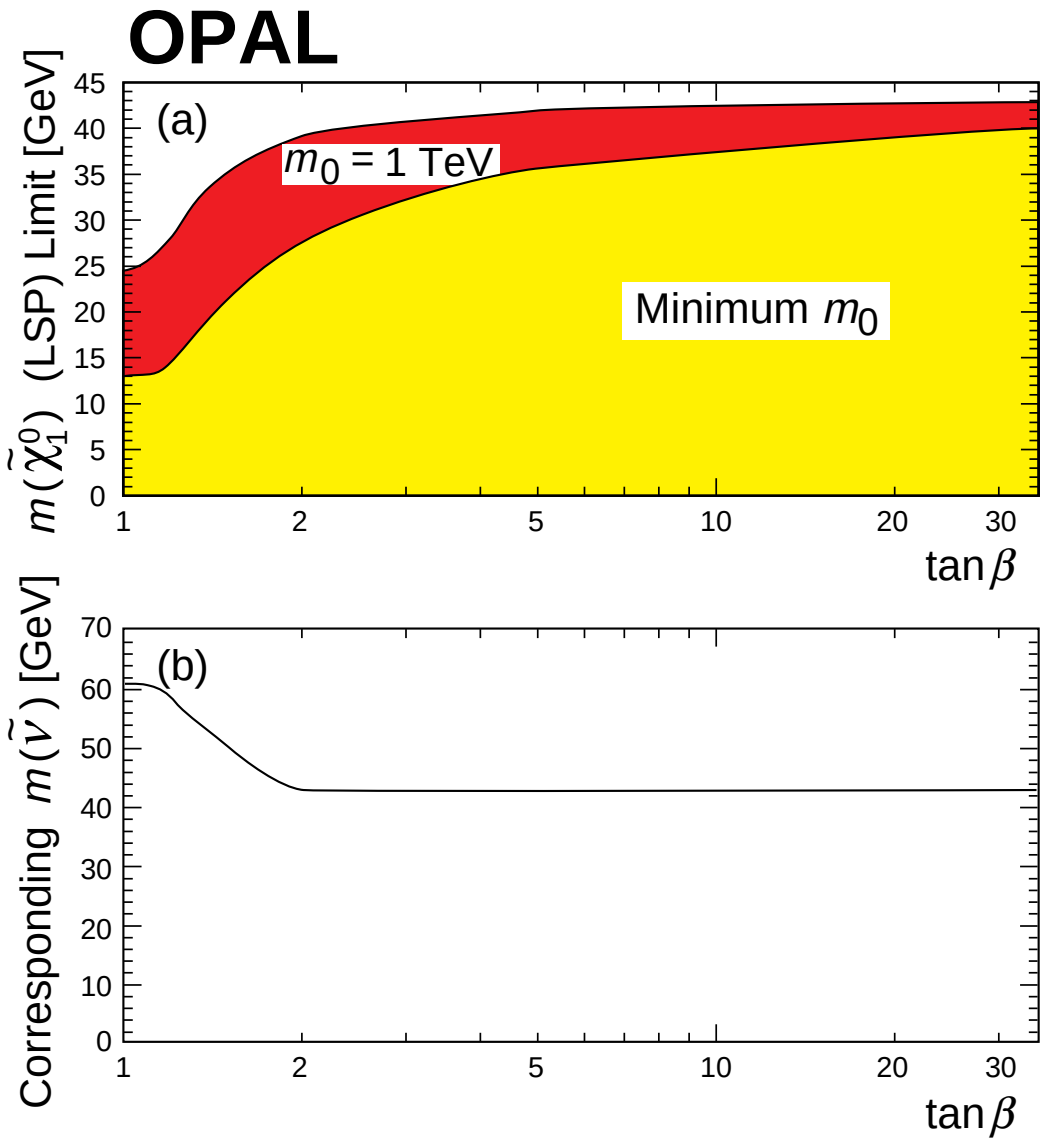

Figure 17: (a) The lower mass limit on the mass of the $\tilde{\chi}_1^0$ as a function of $\tan\beta$ for $m_0 = 1$ TeV and minimum m_0. (b) The value of $m_{\tilde{\nu}}$ corresponding to the minimum m_0 value used as a function of $\tan\beta$.

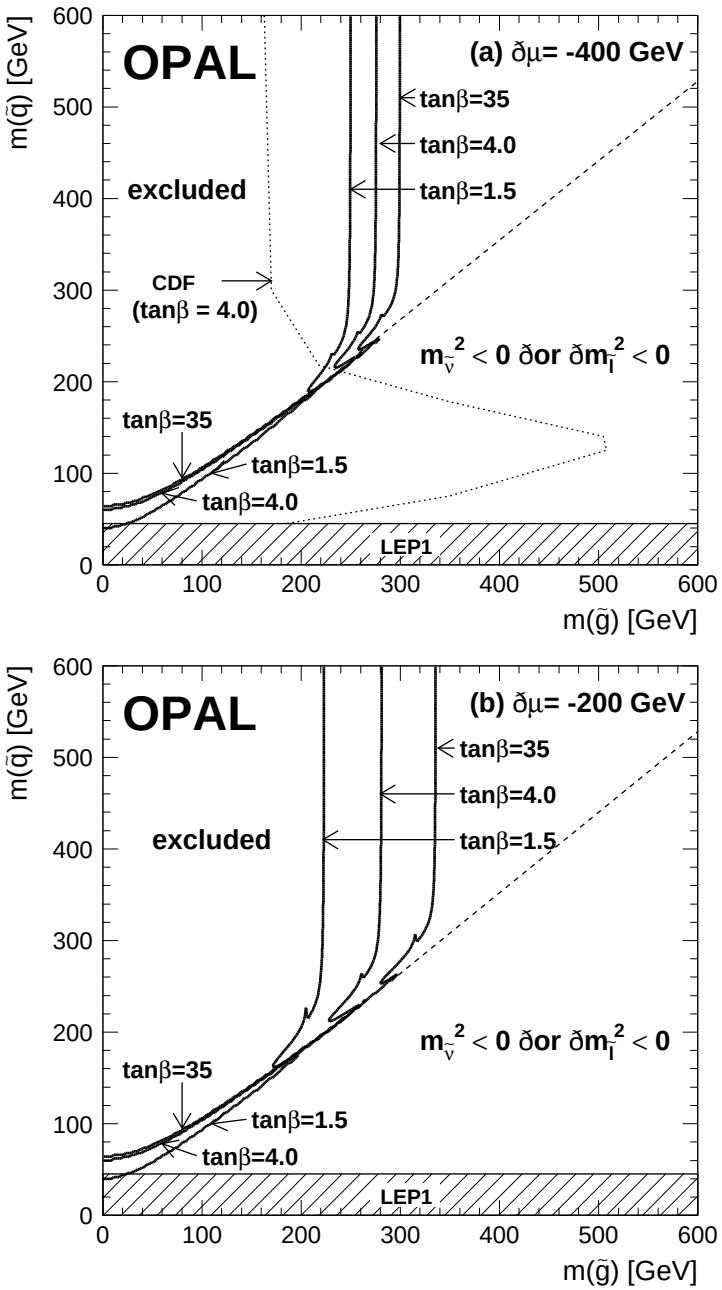

Figure 18: Limits on M_2 interpreted as limits on $m_{\tilde{\mathrm{g}}}$ assuming gauge unification at the GUT scale by using the relation $m_{\tilde{g}}/M_2 = \alpha_s/\frac{\alpha}{\sin^2\theta_W} = 3.5$. $m_{\tilde{\mathrm{q}}}$ is the average of the $\tilde{\mathrm{u}}_R$, $\tilde{\mathrm{u}}_L$, $\tilde{\mathrm{d}}_R$ and $\tilde{\mathrm{d}}_L$ masses and can be calculated from m_0, M_2 and $\tan\beta$ in the CMSSM framework. The limits in the ($m_{\tilde{\mathrm{q}}}$,$m_{\tilde{\mathrm{g}}}$) plane for (a) $\mu = -400$ GeV and (b) $\mu = -200$ GeV thus obtained are shown. The limit in (a) can be compared with the current direct search mass limits on $\tilde{\mathrm{q}}$ and $\tilde{\mathrm{g}}$ from the CDF experiment [40]. The hatched region labelled LEP1 has been excluded by the Z width measurement at LEP1 [36]. In the region below the dashed diagonal line the lightest slepton or sneutrino mass becomes negative within the framework of the CMSSM.